

# A Technical Overview of the CyberKnife System

Warren Kilby, Michael Naylor, John R. Dooley,  
Calvin R. Maurer, Jr. and Sohail Sayeh

*Accuray, Sunnyvale, CA, United States*



CHAPTER FOCUS  
ENGINEERING



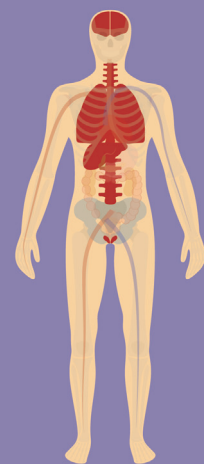
TECHNOLOGY  
ROBOTIC &  
IMAGE-GUIDED



LINK TO  
VIDEO

## ABSTRACT

The CyberKnife System is a frameless, image-guided robotic technology used to deliver stereotactic radiosurgery and radiotherapy anywhere in the body where it is clinically indicated. The treatment procedure is automated and delivered under user supervision. Throughout treatment the radiosurgical target is continually sensed using a combination of X-ray and optical imaging. The target pose is localized into a common reference frame using a combination of image registration algorithms and precisely calibrated coordinate transformations. A robotic couch, on which the patient is positioned, and a robotic treatment manipulator on which a medical linear accelerator is mounted, are aligned using this localization. Manipulation is achieved by delivering ionizing radiation to the target using a high-energy X-ray beam generated by the linear accelerator. Treatment involves delivery of a large number of nonoverlapping treatment beams, from a noncoplanar workspace, that allows sufficient radiation dose to be delivered to the target while respecting the dose tolerances of surrounding healthy tissues. The radiation dose delivered by each beam is determined by a 2D modulated fluence pattern controlled by variable beam collimation, linac dose control, and robot pointing. Pretreatment planning involves segmenting the target and healthy organ volumes using multimodality medical imaging, and using this to optimize the set of beam directions and the modulated fluence pattern for each beam. This chapter describes the CyberKnife System technology, and its major subsystems, as current in 2019.



LUNG



BRAIN



BREAST



SPINE



PROSTATE



LIVER

## 2.1 Introduction

Stereotactic radiosurgery (SRS) is a noninvasive alternative to conventional surgery using precisely targeted beams of ionizing radiation directed from outside the patient to replace the surgical resection of solid tumors, other lesions, or functional targets. SRS was originally developed for intracranial applications and required the use of a stereotactic frame mechanically attached to the patient's skull to achieve the required beam alignment precision. Treatment was delivered in a single session (or treatment fraction) using multiple beams distributed over a large solid angle [1]. Subsequently, the same general principles have been applied with new technologies to treat extracranial targets, either as an alternative to, or in combination with, conventional surgery and radiation therapy. Such extracranial treatment is commonly referred to as stereotactic body radiation therapy (SBRT) [2] or stereotactic ablative radiotherapy (SABR) [3], the subtle distinctions between which are beyond the scope of this chapter. Current SRS/SBRT/SABR (hereafter referred to collectively as *radiosurgery*) techniques use either mechanical frame-based or imaging-based stereotactic alignment, and are typically delivered in one to five treatment fractions. Common clinical indications include intracranial targets [malignant and benign tumors, arteriovenous malformations (AVMs), and functional diseases], spinal tumors and AVMs, and malignancies in the lung, prostate, liver, head and neck, and other sites, including both primary and metastatic diseases [4,5].

A fundamental difference between radiosurgery and conventional radiation therapy is that the former employs more aggressive dose-fractionation schemes. Since all radiation treatment is limited by toxicity to healthy tissues, this requires that radiosurgery achieves higher levels of geometric accuracy and dose conformity than conventional radiation therapy, as outlined as follows.

1. **Geometric accuracy:** The geometric uncertainties associated with aligning external treatment beams to a clinical target volume (CTV) within the body are usually managed by adding margins to the CTV during the treatment planning phase to form a planning target volume (PTV) [6]. Delivering the prescription dose to the entire PTV ensures that the CTV receives the intended dose. The CTV–PTV margin is a combination of setup and internal margins [7]. The setup margin includes the uncertainties in localizing the CTV at the start of each treatment in the same frame of reference as the treatment device, and of aligning the treatment beams to the CTV in this frame. The internal margin accounts for intratreatment motion of the CTV after initial localization. The most common example is respiratory motion, which affects targets within the lung, liver, pancreas, and kidneys. However, clinically relevant internal motion also affects the gastrointestinal and genitourinary systems (e.g., changes in bladder filling or rectal content during treatment can significantly alter the pose of a prostate cancer CTV [8,9]), and for essentially all target locations when gross patient movements are considered. The latter are usually limited by patient immobilization devices, but movements of a few millimeters are observed over typical treatment periods even for immobilized patients with intracranial or spinal CTVs [10]. Accommodating geometric uncertainties using margins is problematic when the CTV is adjacent to radiosensitive healthy tissues (e.g., lung, liver, or brain tissue surrounding a tumor, or the bladder and rectum adjacent to a prostate cancer CTV) since parts of these healthy tissues overlap the PTV and receive the full prescribed dose. These overlaps limit the dose-fractionation that can be employed, especially when complications are associated with relatively small volumes of healthy tissue receiving high doses.
2. **Dose conformity:** The physical nature of radiation transport means that dose deposition cannot be limited to the PTV only, but also spills out into the surrounding healthy tissues. In the standard nomenclature, the volume of tissue receiving the prescription dose is the treated volume (TV), and the volume receiving a dose that is significant in terms of normal tissue tolerance is the irradiated volume (IV) [6]. A perfect treatment would limit the TV to be identical to the PTV and have an infinite dose gradient in all directions beyond the TV such that the TV to IV expansion is zero. Neither of these is practically achievable. The PTV to TV expansion is generally determined by the way in which the incident radiation fluence from each treatment beam is modulated (e.g., by collimating the beam to the precise projection of the CTV using a collimation system that achieves very narrow beam penumbra and very low transmitted fluence outside of the collimated area). The TV to IV expansion is determined by the radiation modality and by the number of treatment beams used and their spatial arrangement. Dose gradients are maximized when many nonoverlapping beams are used. This makes use of noncoplanar beam arrangements distributed across a large solid angle beneficial.

The CyberKnife System provides a method for frameless radiosurgery, enabling treatment to be delivered anywhere in the body where it is clinically indicated. Radiosurgery delivered by CyberKnife is autonomous but delivered under human operator supervision. The treatment paradigm involves a combination of image-based alignment, robotic manipulation of the treatment beam and patient, continual image-based tracking of the target throughout treatment, and use of

a large noncoplanar workspace. This paradigm can be employed anywhere in the body and is used for every treatment delivered by the system. CyberKnife was conceived in 1992 [11] and first fully described in 1997 [12]. The system received FDA approval for intracranial treatment in 1999, which was extended to include extracranial treatment in 2001. To date, it is estimated that over 400,000 patients have been treated worldwide using CyberKnife, covering the full range of clinical indications described above. In the 25 years since its inception the technology has undergone continual development such that almost no component remains unchanged from the original design. A complete technical description of the system was published most recently in 2010 [13]. There have since been major changes to several key subsystems and the introduction of a major new system version. This chapter will therefore provide the first technical overview of the CyberKnife M6 System, as current in 2018.

## 2.2 System overview

The treatment room shown in Fig. 2.1 illustrates the layout of the major treatment delivery subsystems. The patient lies on a flat couch top and except in some pediatric procedures is fully conscious throughout treatment. The couch is supported by a 6 degrees of freedom (6DOF) robotic manipulator that enables the patient pose to be adjusted along all six translational and rotational axes. At the head of the treatment couch is another 6DOF robotic manipulator supporting a medical linear accelerator (linac) that generates the treatment beam. This treatment manipulator allows beams to be directed without the isocentric pointing or coplanar workspace constraints of a traditional C-arm linac gantry. Next to the treatment manipulator is a pedestal in which exchangeable secondary collimator assemblies are stored when not in use. Above the couch are two ceiling-mounted X-ray tubes. These produce square imaging beams directed toward the floor, the central axes of which are each at 45 degrees to the vertical. Image detection is accomplished using two flat panel X-ray detectors mounted flush to the floor. The point in space where the central axes of the two imaging beams intersect is the *machine center*. The treatment manipulator is positioned such that beams can be directed from many noncoplanar directions toward points within a treatment volume, which is a region of space surrounding the machine center. Treatment accuracy relies on the position and orientation of the imaging system with respect to the treatment manipulator being known with high precision, which is ensured by mechanical alignment during installation and calibration procedures performed during system commissioning.

To supplement the X-ray imaging system, an optical imaging system is used for treatments in which respiratory motion is tracked in real time. An array of three optical cameras is installed in a ceiling-mounted boom-arm which can be swung out of the way when not in use. During respiratory motion tracking, the camera is used to continuously measure the position of three optical markers attached to a vest worn by the patient. These major subsystems are described in more detail in Section 2.3.

Because of the radiation hazard of the treatment beam, the system is installed within a shielded bunker. During treatment delivery, the operators (usually radiation therapists) monitor the system from a control room situated outside the treatment room. This control area, as shown in Fig. 2.1, contains the treatment delivery computer. This displays the live X-ray images acquired during treatment and pregenerated digitally reconstructed radiographs (DRRs), target location tracking results, and information about each treatment beam including the dose delivered and beam collimation settings. Once commenced, treatment proceeds autonomously unless errors are detected or the operator pauses delivery. Because the radiation shielding makes it impossible for the operators to view the patient directly the treatment room is fitted with CCTV, and an intercom enables the patient and operators to communicate during treatment. Additional system hardware, including controllers for the two robotic manipulators, linac, and imaging systems, power distribution equipment, linac cooling and gas systems, and a patient database computer, is installed in a separate equipment room close to the treatment room.

The first step in the treatment process is treatment planning, as illustrated in Fig. 2.2. Vendor-provided treatment planning software (TPS) is installed on one or more computers, usually situated in a separate planning office. Each TPS allows a simulation of the treatment delivery in which the optimum geometric arrangement of treatment beams and radiation fluence per beam is determined. The planning process starts with acquisition of a three-dimensional (3D) CT, which is transferred to the TPS via a dedicated patient database. A 3D patient model is built from the planning CT, in which a patient coordinate system is defined and the tissue density at each voxel is calculated. Target volumes and relevant healthy tissues are segmented within this model using a combination of automatic and manual methods. To aid tissue segmentation, multimodality secondary image sets can be registered to the primary CT scan. A virtual alignment of the treatment imaging system to the patient model is then performed, such that the treatment target is close to the virtual machine center. This defines the transformation from the patient coordinate system to the virtual imaging system, and since the imaging system to treatment manipulator transformation is already known, this enables a set of



**FIGURE 2.1** The CyberKnife treatment suite. The left image shows the patient lying on a flat couch mounted on a robotic manipulator, with the linear accelerator mounted on a second robotic manipulator at the head of the couch. In this case the multileaf collimator assembly is shown attached to the treatment robot. Behind the patient and treatment robot in this image is the pedestal used to store the three alternative secondary collimator assemblies when not attached to the treatment robot. The two ceiling-mounted X-ray tubes are shown, with the floor-mounted X-ray image detectors housed under the rectangular green panel beneath the couch. The optical camera array in its ceiling-mounted boom-arm is shown near the left side of the image. The right image shows the control area. The treatment delivery computer to the left displays live X-ray images, DRRs, tracking results, and treatment-related data during treatment. To the right, the CCTV and intercom systems monitor and communicate with the patient during treatment. The small white console next to the keyboard contains low-level controls to initiate and interrupt treatment. *DRR*, Digitally reconstructed radiograph. *Control area image courtesy Dr. J.A. Gersh, Gibbs Cancer Center and Research Institute—Pelham, Greer, SC, United States.*



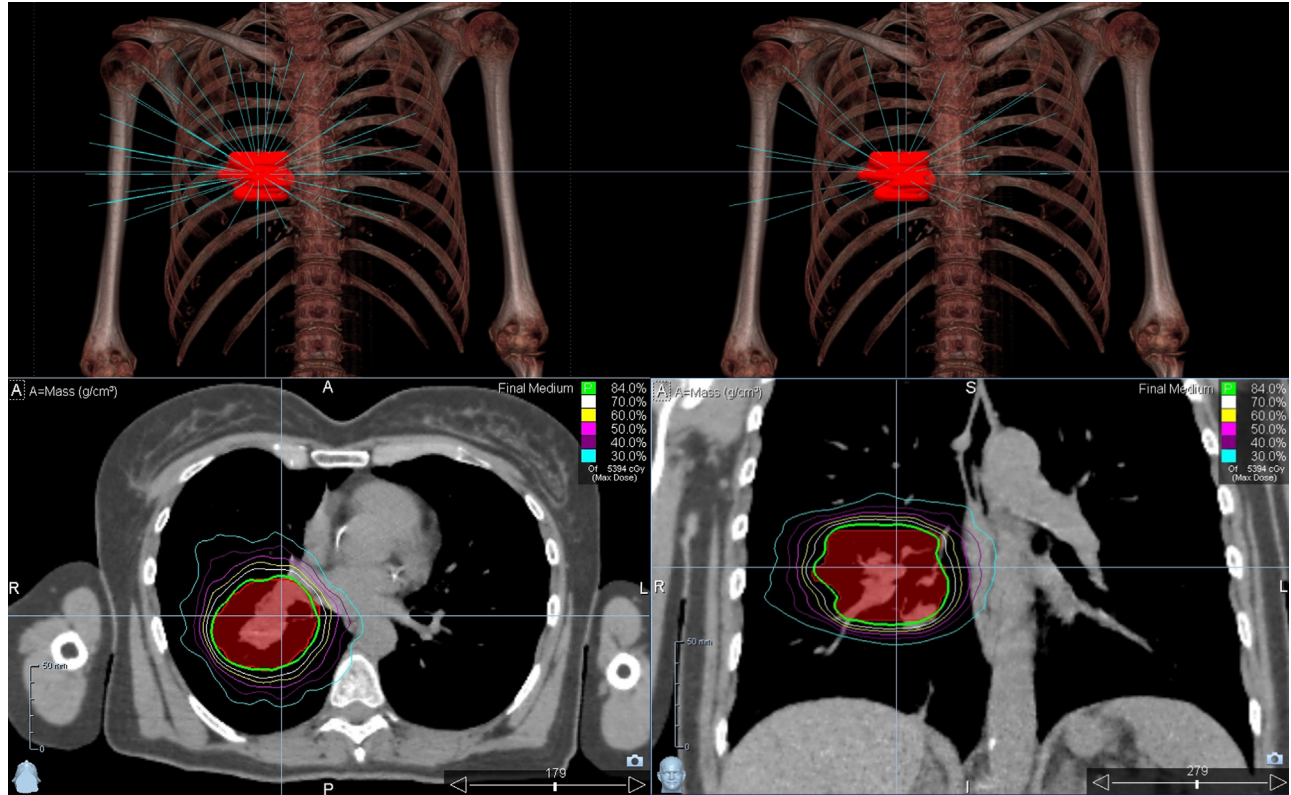


**FIGURE 2.2** An example treatment plan for a lesion in the right lung. Top-left shows an anterior view of the 3D patient model (for simplicity the tissue density has been windowed to show only bone, and the only segmented structure is the PTV, shown in red). The *blue lines* show 100 noncoplanar beam directions that are available to treat this target. Each line corresponds to a position and orientation of the treatment robot relative to the patient that does not violate robot joint, cable management, or collision constraints. Top-right shows the subset of 24 beams which in this case were selected during the treatment plan optimization. The bottom panels show axial and coronal sections of the CT scan. The dose distribution resulting from the optimized set of beam directions and beam fluence is shown by the *colored isodose lines* (connecting points of constant dose). In this case the conformality of the treated volume (within the green line) to the PTV is high, as is the dose fall-off in all directions (shown by the closely spaced *isodose lines* outside the PTV). These are among the dose representations that the treating physician will typically review before approving the plan for treatment. 3D, Three-dimensional; PTV, planning target volume.

virtual treatment beams to be defined onto the patient model corresponding to achievable treatment manipulator orientations. Typically, more than 100 of these feasible beam orientations are found. Using this simulation, the operator selects the optimal set of beam directions and radiation fluence per beam. This complex task is usually performed with the aid of automated optimization algorithms implemented within the TPS. The methods used for image registration, segmentation, dose calculation, and plan optimization are described in more detail in [Section 2.3](#). The resulting dose distribution is reviewed and approved by the treating clinician (usually a radiation oncologist or neurosurgeon) prior to treatment, and the approved plan is stored in the patient database. From the approved plan a set of machine instructions needed to deliver the treatment is automatically generated. In addition, a set of DRRs is generated by ray-casting through the 3D CT model using the simulated orientation of the X-ray imaging system relative to the patient.

Prior to treatment, the plan is transferred to the treatment delivery computer. Treatment alignment is based on registering live stereoscopic X-ray images to the precalculated DRRs generated from the treatment plan. Each 2D image registration is calculated automatically using skeletal anatomy (either skull or spinal vertebrae), lung tumor, or implanted fiducial markers (the details of these registration algorithms are provided in [Section 2.3](#)). The results of the 2D registrations are combined by geometric back projection to give a 3D transformation of the target anatomy in the live images to the corresponding anatomy in the planning 3D model. The registration result contains the change in the target pose (3D position and 3D rotation) within the treatment room with respect to the simulated geometry in the treatment plan. Initially the couch manipulator is adjusted to grossly align the patient, such that these offsets are relatively small (typically a few millimeters and degrees). Once this is accomplished the couch remains static during

treatment, and all fine alignment corrections are achieved by adjusting the treatment manipulator position and orientation from the settings stored in the treatment plan based on the target pose deviation and the known transformation from imaging system to treatment manipulator system. Using the treatment manipulator rather than the couch manipulator to perform the fine alignment is important, as it removes the need for the patient to be considered as a rigid object statically attached to the couch. Intratreatment motion is tracked continually by repeating the cycle of X-ray acquisition—image registration—pose deviation calculation—treatment manipulator correction throughout treatment, typically every 30–60 seconds. The exception to this alignment strategy is for targets affected by respiratory motion, which move too rapidly to be managed at this imaging frequency. In these cases, the optical camera system is used to monitor the position of markers positioned on the patient surface in real time (approximately every 10 ms). Prior to treatment the correlation of external marker positions to internal target positions is calculated using a series of X-ray images acquired at multiple phases of the breathing cycle. During treatment the real-time optical signal is combined with this correlation model to sense the target position in real time, which is used to determine the treatment manipulator corrections needed to track the target in real time and maintain the same static beam-target orientation that was simulated in the treatment plan. Additional intratreatment X-ray images are used to verify and adapt the correlation model throughout treatment. More detail of this respiratory tracking technology is provided in [Section 2.3](#).

The most meaningful definition of geometric accuracy with any radiosurgery system is the *total system error* (TSE) of the entire treatment planning and delivery sequence (a measurement originally developed for frame-based radiosurgery and termed “total clinically relevant error” [14]). With CyberKnife this is most commonly tested using a phantom containing a hidden spherical target object in which two radiochromic films are mounted orthogonally. The phantom is CT scanned using the standard patient protocol, a treatment plan is developed that encloses the target with a conformal spherical dose distribution, and this plan is then delivered to the phantom. The vendor specification for the radial offset between the dose centroid measured on the films and the intended position (center of the spherical target) is  $\leq 0.95$  mm. Versions of this phantom enable the test to be performed for all anatomical tracking methods (skull, spine, lung tumor, and fiducial marker tracking), and with real-time phantom motion to simulate respiratory motion. The TSE combines uncertainties in the full treatment process, including CT acquisition, image segmentation, dose calculation and plan optimization, X-ray to DRR registration, treatment beam alignment, and dose delivery. TSE is measured during acceptance testing and periodic quality assurance tests with every CyberKnife System to demonstrate that this accuracy specification is maintained. A summary of user-published TSE results is provided in tables II and IV of Kilby et al. [13].

## 2.3 Major subsystems

### 2.3.1 Robotic manipulation

#### 2.3.1.1 Treatment manipulator

The treatment manipulator for the CyberKnife M6 System is the KUKA QUANTEC KR300 R2500 Ultra robot. This is a 6DOF robot with a maximum payload of 300 kg, 2496 mm reach, and position repeatability of  $\pm 0.06$  mm. A primary reason for selecting this robot was the higher payload required for the addition of the multileaf collimator (MLC) (described later)—the KR300 has a 60 kg maximum payload increase over the treatment manipulator used in the CyberKnife VSI system [13]. The increased payload comes with a trade-off in overall reach of the robotic arm—approximately a 200 mm reduction in maximum reach. This required changing the treatment room layout in two ways. First, the robot was moved from 45 degrees superior-lateral to the patient to be in-line superior to the patient. Second, a custom pedestal was designed to raise the robot 412 mm off the floor, allowing the system to reach over the patient and maximize the available workspace for delivery.

Cable management, predominantly to support the operation of the linac and other devices in the treatment head, as well as industrial design are added to the KUKA robot ([Fig. 2.3](#)). The conduit for the cable management is 95 mm in diameter and carries dozens of cables including sensors for beam collimation systems, power and signal cables for the monitor chamber and dosimetry electronics, a pneumatic air hose, and high-energy cabling for the linac. The cable management is designed to support the full range of robot motion throughout its workspace—this results in a 750 mm extendable range of the conduit when the robot is stretched out, but also requires that the cabling retracts when the robot head is superior to the patient. A tensioning mechanism is located at the elbow joint to ensure that the cabling is retracted as needed while maintaining minimum bend radii in all cases.



**FIGURE 2.3** The treatment robot showing the KUKA robot, treatment head, cabling and tensioning mechanism, and pedestal (left), and in the treatment room with industrial covers fitted together with the treatment couch and Xchange table (right).

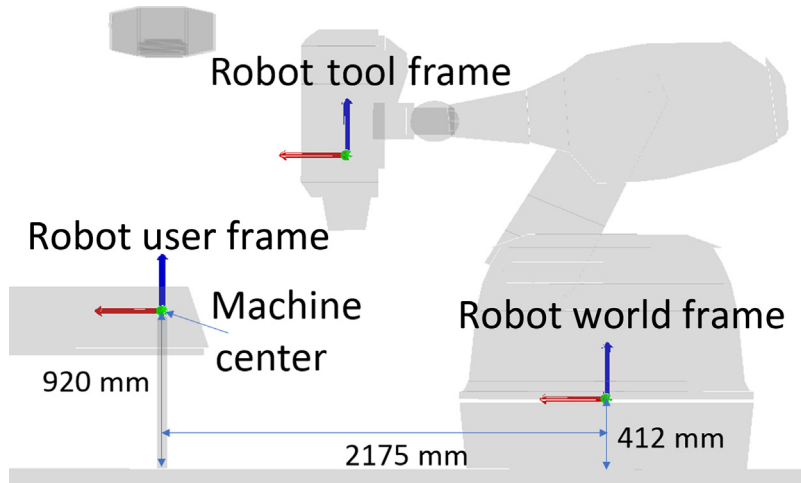


**FIGURE 2.4** Lateral view of robot system coordinate frames. Red is +X, blue is +Z, and green is +Y.

### 2.3.1.2 Coordinate systems and treatment workspace calibration

There are three primary coordinate frames when describing the robot workspace within the treatment room (Fig. 2.4). The robot world frame has its origin at the base of the robot, centered on the first axis of rotation where the robot is mounted on top of the pedestal. The robot tool frame is defined by a laser mounted inside the linac, such that the laser is coincident with the radiation beam, and the origin is the treatment X-ray beam source (center of the linac target). The robot user frame is defined with its origin at the machine center, with rotations aligned to the robot world frame.

The treatment volume for the CyberKnife is centered at the machine center. This point is nominally 2175 mm + X and 508 mm + Z in the robot world frame—when combined with the pedestal, this gives a height of 920 mm off the floor. To calibrate the exact position of this point relative to the robot, a calibration post is inserted into a floor frame

which provides a reference point. The calibration of the robot relative to the machine center is performed using the linac laser to scan across a point like photodetector located at the tip of the calibration post. Scans of this point are performed from positions throughout the robot workspace and a least-squares minimization is found which provides the calibrated robot tool frame and origin of the user frame at the calibration point.

This provides a baseline calibration for the robot. However, to reach submillimeter accuracy throughout the entire clinical workspace, additional calibrations are required. [Section 2.3.1.3](#) discusses the discretization of the workspace into “paths” and “nodes,” as well as the next steps in system calibration.

### 2.3.1.3 Treatment paths and node properties

The available workspace that the robot can reach for clinical use is discretized into specific points, referred to as nodes, which are grouped into larger sets, referred to as paths. The robot can be oriented such that the treatment beam source (center of the linac X-ray target) is coincident with each node, and therefore nodes represent the source positions of treatment beams. Nodes are selected from a set of points located on concentric spheres about the machine center, with radii [referred to as source-to-axis distance (SAD)] ranging from 650 to 1200 mm. The node positions are selected to maximize robot reachability during real-time tracking of patient motion, as well as to provide flexibility for robot traversals to other nodes while avoiding collisions in the room and ensuring that the cable management is not stretched or compacted too much.

Separate paths are defined for different target anatomy and collimator types. The “head” path is designed such that the head portion of the couch top is located at the machine center. This is a smaller volume of the couch and leaves the section of the room between the couch top and the robot base open for treatment nodes. [Fig. 2.5A](#) shows the position of nodes in this path. This path has shorter SAD nodes (650–900 mm) to maximize the effective dose rate. The extracranial “body” path is designed for the couch extended fully superior to support placement of targets in the thorax or abdomen at the machine center. This path has longer SAD nodes (800–1200 mm) to allow for larger patient clearance due to respiratory motion tracking, prostate pitch tracking, and the larger range of possible alignment positions throughout the entire body (rather than just the center of the skull for the head path).

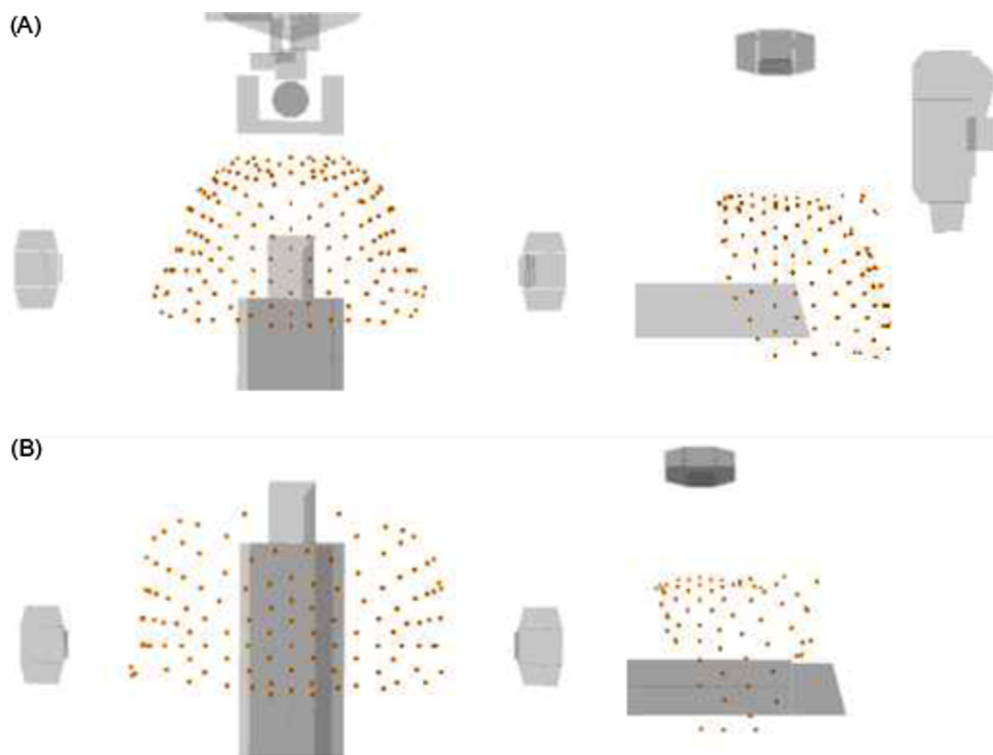


**FIGURE 2.5** (A) Head path, seen from above (left) and from the side (right). Each red dot is a node. (B) Body path seen from above (left) and from the side (right). Each red dot is a node.



Although the fixed collimator housing and Iris collimator have the same external geometry, the MLC is very different, requiring different paths to handle this distinction (see [Section 2.3.2](#) for a description of these secondary collimators). This results in four primary clinical paths, excluding those used for quality assurance. Each of these paths is calibrated independently, including separate calibrations for the fixed and Iris collimators due to mass differences. Path calibration consists of moving to each node in each path and performing a scan of the calibration post with the linac laser. This process generates a list of offsets which is applied at the delivery time. A final correction offset is measured using an arrangement of treatment X-ray beams directed at the machine center, to a phantom containing orthogonal X-ray-sensitive films (the TSE measurement described in [Section 2.2](#)). This combination of calibrations allows the system to achieve submillimeter accuracy in treatment beam delivery.

The path sets for the CyberKnife M6 System include 117 clinical nodes for the “body” Iris and fixed collimator path, 179 for the “head” Iris and fixed path, 102 for the “body” MLC path, and 171 for the “head” MLC path. These nodes, used as source points for delivering radiation, are referred to as “dose nodes.” Each path also contains “dummy nodes” which are used only as traversal waypoints. Each node has associated data to inform the system how that node may be used from treatment planning through treatment delivery. This information includes maximum rotational and translational tracking corrections, X-ray imaging status (i.e., whether placing the treatment head at the node causes the treatment robot to obstruct one of the X-ray imaging systems), and a list of nodes in the path to which the robot can safely move, as well as an associated traversal time. The maximum tracking corrections guide the treatment planning system (TPS) to utilize the proper set of nodes given the parameters of the plan being created. For example, nodes used in prostate treatments require additional robot reachability to support  $\pm 5$  degrees of pitch correction, above the standard  $\pm 1.5$  degrees, while nodes used with real-time respiratory motion tracking must support  $\pm 25$  mm of translation corrections rather than the standard  $\pm 10$  mm. The X-ray imaging status of nodes is used to order the nodes appropriately so that there will be guaranteed imaging opportunities where the robot is not blocking either of the X-ray imaging devices. Once the dose nodes are selected during treatment planning, this provides the information required to do a traveling salesman optimization which minimizes the time spent moving between them. The traveling salesman algorithm is based on the Lin–Kernighan heuristic [15], but simplified and customized to work with the constraints and parameters for CyberKnife—primarily ensuring that imaging nodes are visited based on a custom time interval defined by the operator.

#### 2.3.1.4 Collision avoidance and proximity detection

Although the paths were designed to avoid collisions with other components of the system, as well as a large bound on the patient volume, the system continuously monitors the position of each robot (treatment robot and patient couch) and calculates distances between these moving objects versus other moving components and static obstacles in the room. All objects are modeled as adjoining convex polytopes for the purposes of the proximity calculations. [Fig. 2.6](#) shows an example of the polytopes when the robot is at a superior head path node, the colors are only to differentiate between separate models. It is important to note that the couch position can only act as a guide for the patient position, and depending on setup factors (pillows, blankets, pads, etc.), the patient may not be in the exact, expected position. The user can define one of a set of standard avoidance volumes around the couch based on the patient size and setup. The patient-facing portion of the collimator housing is also encased in a touch sensor so that if the patient reaches out to touch the robot, or there is a collision, an interlock is tripped that stops motion.

#### 2.3.1.5 Xchange table and tool mounting calibration

One feature of the CyberKnife System is exchangeable secondary collimators via a pneumatic tool-changing mechanism. This enables rigid mounting of the linac and accurate calibration of the robot, while enabling the use of up to three different secondary collimation devices. To enable automated secondary collimator exchange, the storage table must be located and calibrated with respect to the robot. The tool-changing mechanics require submillimeter accuracy to operate, which requires a full 6DOF calibration of the table coordinate frame and sensor positions. The table has spots for three calibration posts, which are smaller versions of the one used for primary system calibration, and the calibration process moves the robot through a vertical and horizontal scan of each post. This provides three points, giving a full 6DOF representation of the table top plane relative to the robot. At the center of the storage well for each secondary collimator is another sensor. Each of these is scanned with the linac laser to calibrate the center of the well. In turn, the robot picks up and drops off each housing to ensure that the calibration scans successfully found the center positions. The bottoms of the wells are spring loaded, with overtravel sensors to monitor if the robot pushes down too far—while the tool mounting face of the linac has sensors to determine when a physical connection is made.

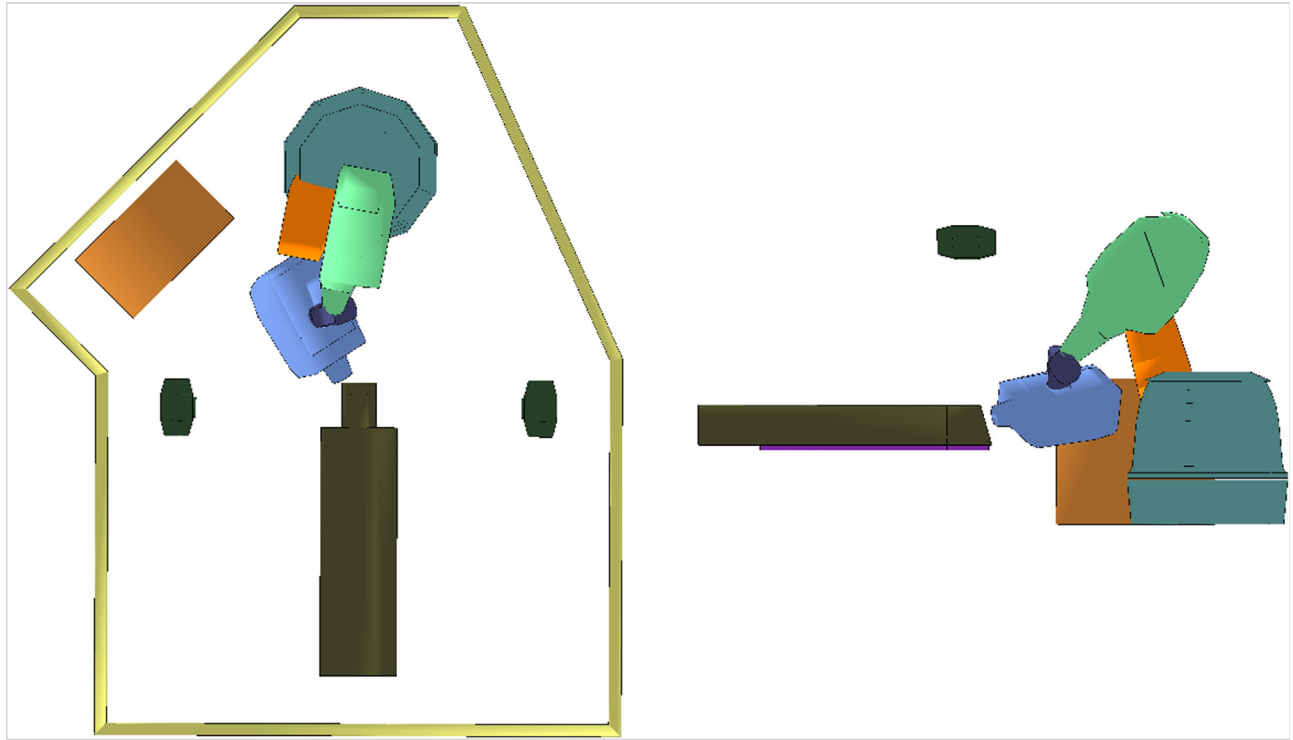


**FIGURE 2.6** Example view of proximity detection modeling, with static and dynamic modeled components. The patient avoidance area around the couch is not shown.

The combination of the calibration procedure and these sensors allows the system to safely and quickly exchange between the different secondary collimators.

In addition to enabling the use of multiple collimator types, the table also enables the system to perform a laser alignment check prior to each treatment. This occurs either through a successful exchange of collimators or a single check of the laser value over the center of one of the housing wells. As the linac laser is aligned and calibrated with the treatment beam, this simple check ensures that the treatment beam is aligned consistently. This is checked prior to each treatment delivery.

### 2.3.1.6 RoboCouch

The patient couch (RoboCouch) is also a serial link manipulator which brings additional functionality to the CyberKnife System. RoboCouch is a custom-designed robot, based on the selective compliance articulated robotic arm (SCARA) configuration, which utilizes the same KUKA controller and KUKA wrist as the treatment robot. The first axis is a vertical axis to provide Z motion, with the two subsequent axes providing planar X/Y motion, followed by a three-axis intersecting wrist to enable rotation positioning (Fig. 2.7).

This design enables a therapist to fully align a patient in all 6DOF without having to physically adjust the patient inside the treatment room. The design of the couch provides the user with the ability to treat patients up to 500 lb, while maintaining submillimeter accuracy. The RoboCouch workspace allows for 100 cm of travel in the inferior/superior direction, while extending  $\pm 18$  cm in the patient left/right direction, and a minimum load height of  $\leq 55$  cm off the floor, which equates to 37 cm of travel posterior to the machine center. This workspace also includes nominal rotation ranges of  $\pm 5$  degrees about each axis, although there are reduced limits at the exterior of the translation limits. The combination of couch limits with the treatment robot tracking limits allows the CyberKnife flexibility with initial patient position on the couch, as well as to handle large patient movements without frequent manual adjustments of the patient.

The RoboCouch is calibrated to the rest of the CyberKnife System by performing a sequence of couch moves and tracking calibration targets using the X-ray imaging system. By correlating native couch coordinates to the imaging system coordinates, the system can accurately adjust the patient position based on imaging system results to maintain

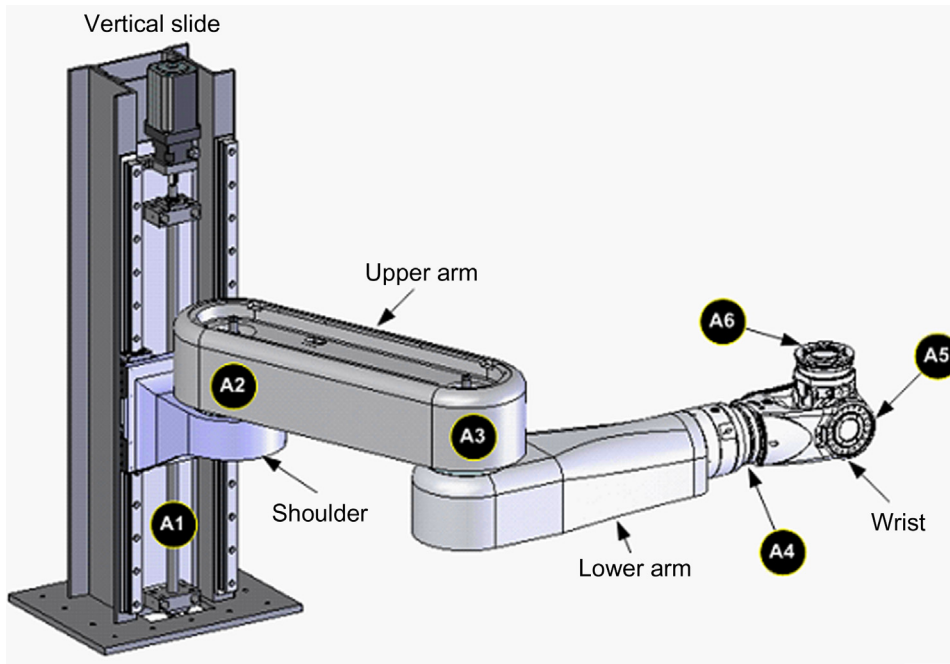


**FIGURE 2.7** RoboCouch high-level diagram with axis labels.

patient alignment about the machine center. Once this calibration is performed, the CyberKnife utilizes the couch to adjust the patient position to nominal alignment with the DRRs, and then allows the treatment robot to adjust on-the-fly as the patient moves during treatment delivery.

### 2.3.2 Treatment head

The treatment head produces and controls the X-ray treatment beam. In the following description “up” is the direction along the beam central axis away from the patient, and “down” is toward the patient. The treatment head is mounted to the treatment manipulator and is divided into two parts (Fig. 2.8). The upper part is permanently attached, and the lower part is mechanically exchangeable for one of three alternatives. These lower head assemblies are stored in a pedestal next to the treatment robot base (Fig. 2.1) and are exchanged automatically by the treatment manipulator using a pneumatic tool-changing mechanism as described in Section 2.3.1.5.

The fixed (upper) part of the treatment head contains the linac which generates the treatment beam by accelerating electrons along an evacuated accelerator structure using microwave power, and colliding these accelerated particles with a thin metal target to generate X-rays principally through bremsstrahlung interaction. The linac is powered by an X-band cavity magnetron, also mounted in the treatment head, and delivers a 6 MV X-ray beam with a dose rate of 1000 cGy/min at the reference treatment distance of 800 mm from the beam source. The X-ray target is situated within the primary collimator, which is a large tungsten enclosure designed to minimize radiation leakage in all directions except along a fixed rectangular aperture defining the maximum possible treatment field size. Downstream of the target is the monitor chamber, which is a sealed, gas-filled ionization chamber used to control the dose delivered to the patient. Charge measured in this chamber is proportional to the X-ray fluence emitted by the linac. The relationship between this charge measurement and dose delivered to the patient is carefully characterized when the system is commissioned. During treatment, this signal is used to terminate each treatment beam when the radiation dose specified in the treatment instructions has been delivered. In addition, the chamber monitors the treatment dose rate, beam uniformity, and beam symmetry, and terminates treatment if these deviate outside a tolerable range. The laser–mirror assembly is aligned to direct the beam from a low-power optical laser mounted at right angles to the treatment beam along an axis coincident with the center of the radiation beam. The laser is not used therapeutically, but is essential for various quality assurance and calibration procedures and as part of the assembly exchange mechanism described previously.

The detachable part of the treatment head contains the secondary collimation system that defines the shape of the treatment beam incident on the patient. At the top of each of these is an intermediate collimator. This is fixed tungsten

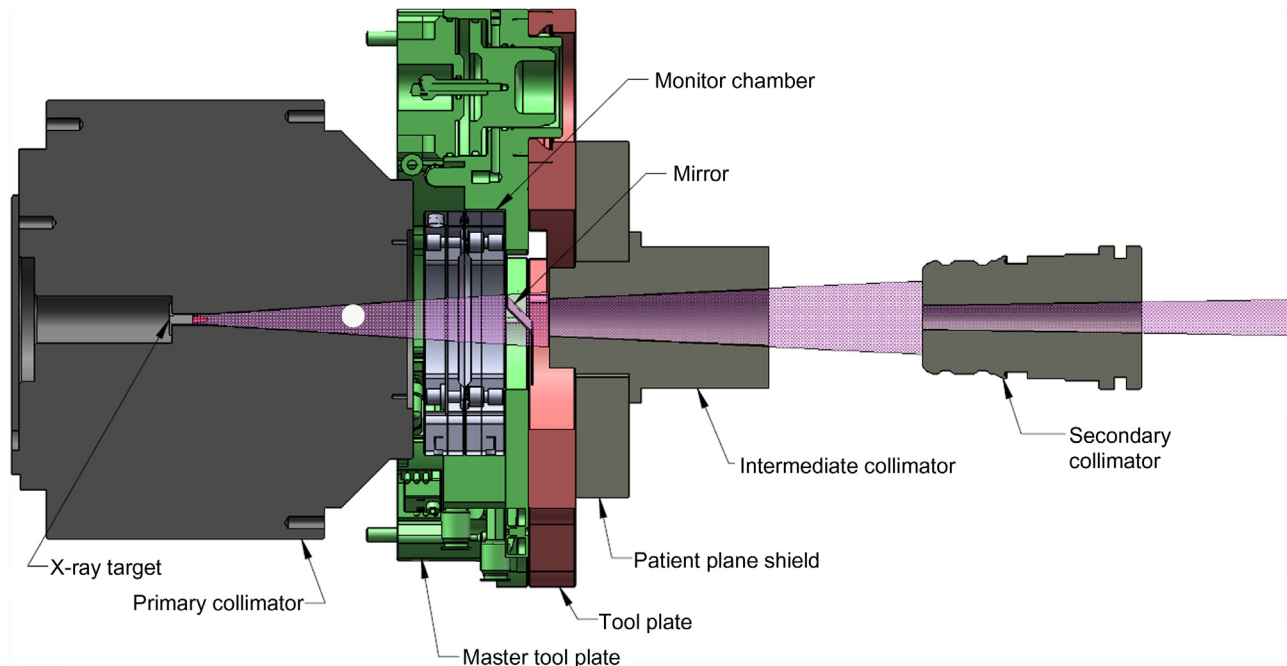


**FIGURE 2.8** A section of the treatment head showing the major components responsible for shaping and controlling the treatment beam. The linear accelerator (not shown, to the left of this figure) directs a beam of electrons accelerated to approximately 6 MeV onto the X-ray target where they interact to generate the X-ray beam shown in purple. This beam is collimated by the combination of primary, intermediate, and secondary collimators to shape the beam that is incident on the patient (not shown, to the right of this figure). The electric charge created by the beam as it traverses the gas-filled monitor chamber is used to control the dose delivered to the patient. The 45 degrees mirror directs a low-power laser beam (not shown) that is coincident with the beam central axis. This is used for various quality assurance and other functions, but is not involved in treatment delivery. Automated pneumatic connection and disconnection of the master tool plate to tool plate allows alternate secondary collimator assemblies to be attached for each treatment. The fixed collimator assembly shown here is the simplest of these assemblies. The alternate secondary collimator assemblies (not shown) are an Iris variable circular aperture collimator, and a multileaf collimator.

shielding designed to reduce the field size from the maximum defined by the primary collimator down to the maximum supported by the variable secondary collimation sitting below, and to provide some additional shielding to the primary collimation. The three secondary collimator assemblies are described next.

1. Fixed conical collimators. These are 12 static tungsten cylinders, each with a circular aperture. The apertures define beam diameters (at 800 mm from the source) of 5–60 mm. The two smallest sizes have straight apertures. The others are focused to the beam source, which is important to achieve a sharp beam edge (i.e., to minimize the beam penumbra). The individual collimators are manually fitted within the fixed collimator assembly. The collimator size is sensed by the delivery system and an interlock prevents treatment delivery unless this matches the size contained in the treatment plan for each beam.
2. Iris variable aperture collimator. This collimator can replicate the same set of 12 circular field sizes as the fixed collimators without the need for any manual exchange of parts. It is formed by 12 triangular tungsten segments divided into two banks of six, mounted one above the other. Each bank defines a hexagonal beam aperture, and the two banks are rotated through 30 degrees with respect to each other to achieve a dodecagonal beam that closely approximates a circle. The rotational offset between the two banks also minimizes the radiation leakage between the segments, since any gap between segments in one bank is shielded by the body of a segment in the other. The upper bank forms a smaller aperture than the lower one to approximate the focusing of the fixed collimators. All 12 segments are driven using a single motor. This collimator assembly is described in greater detail elsewhere [16].
3. InCise MLC. This collimator can form irregular beam shapes within a maximum aperture of 115 mm × 100 mm (projected at 800 mm from the source). The beam collimation is provided by 52 tungsten leaves, divided into two opposing banks of 26, which move along linear trajectories orthogonal to the beam central axis. The leaves are driven independently and are capable of unlimited interdigitation and overtravel. The edges of the treatment beam are collimated either by the tips or sides of the leaves. To minimize beam penumbra, the leaf tips have a three-sided design such that they are focused at the target when the leaf is fully open, fully closed, and at the beam center, with



a compromise made at other positions. The leaves are flat-sided and thicker at the bottom than at the top, meaning that the sides are focused at the target. However, to minimize interleaf radiation leakage the entire leaf assembly is rotated by 0.5 degrees, which achieves a compromise between penumbra and leakage. A detailed description is provided elsewhere [17].

The secondary collimator selection is made during treatment planning. Generally, fixed collimators are preferred for treatments of very small targets such as trigeminal neuralgia, because they deliver the sharpest beam penumbra and avoid any aperture size uncertainty. The Iris collimator is generally preferred for treating larger target volumes with circular apertures since it allows multiple beam diameters to be combined without the need to manually exchange fixed collimators during treatment. The combination of multiple aperture diameters confers both a treatment time and dosimetric advantage over fixed collimators in many cases [16]. The MLC is the most flexible of the collimator options, allowing arbitrary noncircular apertures and larger apertures than are possible with the other options. This flexibility makes MLC treatments generally the fastest to deliver and can also result in dosimetric advantages, although the radiation transmission and mechanical positioning tolerances are larger than with the other collimators. Treatment plans can be generated for multiple secondary collimator options and compared during the planning phase to inform this decision, or it can be based on prior clinical experience of similar cases.

### 2.3.3 Imaging systems for treatment delivery

CyberKnife includes both X-ray and optical imaging systems. The former uses two ceiling-mounted X-ray tubes with beams tilted at 45 degrees to the vertical. This provides an orthogonal stereo image pair from which the 3D location of image features can be obtained. X-ray techniques from 40 kV to 150 kV are available. The X-ray beams project a fixed field size of approximately 15 cm × 15 cm at the machine center. The nominal distance from the X-ray source to the machine center is 2.2 m, as is the distance from the machine center to the image detector, giving a magnification factor of two. The image detectors are mounted at floor level under load-bearing covers. Each detector is a CsI scintillator deposited onto an amorphous silicon photodiode with a detection area of 40 cm × 40 cm divided into 1024 × 1024 pixels. The entrance surface dose [18] at the machine center for a typical chest exposure (120 kV, 11.5 mAs) is 0.21 mGy. After images are acquired for initial patient alignment the user specifies the interval between subsequent image acquisitions which are used to detect and correct for intrafraction target motion. This interval is typically set at 30–60 seconds. For a lung radiosurgery treatment delivered in three fractions, 138 image pairs might be acquired in total. Using the entrance surface dose per image, the total effective dose delivered by the imaging system during this treatment estimated using the methods in Ref. [18] is 2.6 mSv, which is lower than that from a diagnostic chest CT [19–22].

The optical imaging system, which is used in combination with the X-ray system during respiratory motion tracking, consists of three cameras in a ceiling-mounted retractable boom-arm. This camera array detects the position of three optical markers attached to the patient surface. Each marker is the tip of an optical fiber, with the other end connected to a red LED. The LEDs are pulsed sequentially (i.e., marker 1, then 2, then 3) so that they can be differentiated by the camera, which reads their positions at about 100 Hz. The camera controller calculates each marker position in a 3D camera frame, which is later reduced to a scalar measurement along the marker principal axis of motion for use in the internal–external correlation model that is described later. This system operates in normal room lighting conditions.

### 2.3.4 Target localization and tracking methods for treatment delivery

#### 2.3.4.1 Registration of live X-ray images and digitally reconstructed radiographs

As described in Section 2.2, the basis for target localization and tracking during every CyberKnife treatment is automatic registration of live X-ray images acquired continually throughout treatment (typically every 30–60 seconds) to DRRs generated from the treatment planning CT image in which the position and orientation of the treatment beams are known. Four image registration methods are available.

#### 6D skull tracking

This method involves tracking the skeletal features of the skull, and is used for intracranial and some upper cervical spine and head and neck targets. Prior to treatment a library of DRRs is calculated, simulating different patient *roll* angles (i.e., rotation of the planning CT image about the patient superior–inferior axis), which is the rotation out-of-plane for the X-ray images. First, each live image is rigidly registered to the corresponding zero roll angle DRR using an intensity-based image similarity measure and a multiresolution search (from coarse to fine spatial resolution), from

which the 2D transformation (two translations and in-plane rotation) is estimated. Next this transformation is used to align the live image with the set of DRRs with varying roll angle, sampled every 1 degree, and this set is searched using a different image similarity measure to estimate the roll angle. The in-plane transformation and out-of-plane roll angle are fine-tuned in a similar two-step iterative process, with each estimate providing the starting point for the next iteration, but using more accurate and computationally expensive methods and finer roll angle resolution. The final rigid 3D transformation is calculated by geometric back projection of the two 2D results, with the roll angle averaged between the two 2D results. A complete description is given by Fu and Kuduvali [23].

### Xsight spine tracking system

This method is used for targets located within the spine or those fixed relative to it. During treatment planning a tracking volume is segmented which typically contains the three spinal vertebrae closest to the target volume, and registration with the live images is performed using only the tracking region corresponding to this volume of interest (VOI) projected in each DRR. While superficially a similar problem to skull tracking, spine tracking is complicated by two main factors: (1) overlying high-contrast anatomical structures within the CT and live X-ray field of view (e.g., ribs, clavicle) may deform relative to the vertebrae (e.g., due to a change in arm position, or breathing) changing the image intensity within the tracking region observed in the live images from that simulated in the DRR, (2) the vertebrae within the tracking volume can deform relative to each other. The principal changes in the spine registration method versus skull are that (1) the tracking DRR is calculated by ray-tracing only through a spine volume segmented in the planning CT, so it only contains information related to the spine and not overlying tissues, and (2) rather than one global 2D–2D registration of the tracking region within the tracking DRR to the live image, this registration is performed using a grid of “nodes” distributed within the tracking region. The displacement of each node between the live image and the tracking DRR is calculated independently using an intensity-based similarity measure within a small image sub-region surrounding the node, and the node displacements are combined with smoothness constraints to estimate a rigid transformation of the target in each projection. The 2D registration results are combined by back projection to estimate the 3D transformation, and the out-of-plane roll angle is estimated by comparison of the 2D images to a library of precalculated DRRs with varying simulated angles. Details are provided in Refs. [24–26].

### Fiducial marker tracking

This method requires implantation of radiopaque fiducial markers (usually metal seeds, coils, or clips) within or adjacent to the target volume. Typically, this is used for soft-tissue targets not fixed relative to the skull or spine such as prostate, liver, pancreas, and breast. Marker implantation is usually performed percutaneously under image guidance, although lung fiducials can also be implanted bronchoscopically [27,28]. A minimum of three fiducials are needed to calculate translations and rotations, and typically three to five are implanted (one study has shown there is little benefit to implanting > five [29]). During planning, the markers are localized within the CT image and tracking is performed by registering these known features in the DRRs with corresponding features in the live images (algorithm details are provided in Refs. [30–32]). There is a risk of fiducial migration between planning CT and treatment delivery leading to treatment inaccuracy. To mitigate this the planning CT is usually acquired at least 1 week after implantation to allow the markers to fixate. In addition, migration changes the intermarker distances between the live image and DRR, and the system provides tools to identify these changes and omit individual markers from the registration calculation if needed.

### Xsight lung tracking system

While fiducial marker tracking can be used for lung tumors, this is often undesirable due to the risk of the pneumothorax during percutaneous marker implantation. Fortunately, the radiographic contrast between the tumor and surrounding low-density lung tissue is large enough to enable fiducial-less tracking in a proportion of patients. Xsight lung tracking is performed in two stages. The first is alignment of the patient using Xsight spine tracking of the spinal vertebrae closest to the lung tumor in the planning CT. This is used to adjust the treatment couch to place the estimated lung tumor location near the center of the imaging field of view, and is also used to rotationally align the patient. This step is performed only once, at the start of treatment. The second step is to register the live images to the corresponding DRRs using the image intensity associated with the tumor itself, and this step is repeated for every live image acquired during treatment. The algorithm used to solve this soft-tissue image registration problem has evolved through three major generations. In all cases a tracking volume that encapsulates the lung tumor is defined in the planning CT, and the projection of this VOI onto each DRR, the tumor template, is used to calculate the registration with the live image.

The original Xsight lung algorithm was released in 2006 [33]. The second-generation algorithm released in 2009 contained incremental improvements on this method, which extended the algorithm success rate (the proportion of the patient population for which the algorithm successfully tracked the tumor) [34]. The third-generation algorithm, released in 2011, uses a fundamentally different approach to the two earlier versions. As in the second version, the tumor template DRR is generated by ray-tracing through a subvolume of the planning CT that contains only the immediate region around the tumor. However, rather than considering this template as a single rigid structure to localize in the live image, the template is divided into overlapping patches, each only a few millimeters square. Patches are registered to the live image independently using a localized intensity similarity measure (normalized cross-correlation). Only patches which have a strong correlation with their locations in the full CT DRR (i.e., those expected to give a strong correlation between features in the tumor and corresponding features in the live X-ray image) are used. Furthermore, the intensity standard deviation within each patch is used to weight the registration result when all of the patch registrations are combined (i.e., more importance is given to patches that include clearly identifiable features). Finally, this weighted sum of individual 2D patch registrations is used to calculate the 2D registration for the whole tumor template, and the two image projection results are back-projected to give the 3D transformation. Dividing the registration problem into a set of smaller patch registration problems makes the method more robust in the presence of tumor rotation and deformation during breathing, and makes it less sensitive to differences between DRR and live image intensity (e.g., due to variations in X-ray technique or image detector nonuniformity) since a local image similarity measure can be used that is normalized to the intensity variation within that patch, and allows the registration to be calculated using only those parts of the tumor template that contain identifiable features that correlate well with the tumor as projected in the full DRR.

In some cases, it is possible to localize a lung tumor in one X-ray projection but not the other (usually because in one projection the tumor is superimposed on the mediastinum or spine). Therefore the system provides a *1-view* tracking mode in which Xsight lung is used to track the tumor only in one projection, and the positional uncertainty normal to this projection is accommodated using a larger PTV margin in that direction only. This additional margin can be informed using a 4D-CT study. It is important to note that the X-ray system geometry means that the superior–inferior tumor position, which tends to represent the largest component of respiratory motion, is detected in both X-ray projections. In other cases, particularly if the tumor is very small, it might be impossible to localize it in either projection. Therefore a *0-view* tracking option is available, in which case the initial spine alignment is used to localize the tumor, and the positional uncertainty associated with untracked respiratory motion is accommodated in a larger PTV (Fig. 2.9). For these patients, fiducial tracking is also an option. The CyberKnife System provides a lung treatment simulation mode which allows the patient to be imaged and the feasibility of 2-view, 1-view, or 0-view tracking to be established before the treatment plan is generated. Retrospective analysis (previously unpublished) of image data from 100 lung tumors treated using fiducial marker tracking in 94 patients shows that the third-generation Xsight lung algorithm could be used in 2-view mode for 64% of cases (increased from 45%, and ~20% with the second- and first-generation algorithms, respectively); 1-view tracking was possible in 81% of cases using the third-generation algorithm.

#### 2.3.4.2 Real-time respiratory motion tracking

Section 2.3.4.1 describes methods for localizing the tumor (or tumor surrogate) in live X-ray images acquired typically every 30–60 seconds. These methods are useful for tracking quasistatic tumor motion (i.e., tumors that move infrequently, or with a period that is much longer than 1 minute), but are not sufficient for tracking tumors that move due to respiration. Continually acquiring X-ray images at the frequency required to track respiratory motion throughout treatment is undesirable because of patient dose. Therefore the Synchrony Respiratory Motion Tracking System is a hybrid method which relies on the correlation between external marker positions on the patient surface (monitored optically in real time) and tumor position (monitored by X-ray imaging every 30–60 seconds). Unlike gating or breath-hold methods, this tracking approach maintains a 100% duty cycle (i.e., treatment is delivered continuously during all phases of breathing) and allows the patient to breath normally throughout. The robotic treatment manipulator provides an ideal platform for respiratory motion tracking, unique to the CyberKnife System, because it allows the entire treatment head to follow the 3D tumor trajectory in real time. Alternative experimental approaches for real-time tracking suffer disadvantages in comparison, namely (1) tracking by real-time beam reshaping is possible with an MLC but not circular collimators, and has limited tracking resolution in the direction normal to MLC leaf motion and no ability to track motion parallel to the beam central axis, and (2) tracking by real-time couch motion requires that the patient is assumed to act as a rigid body statically attached to the couch during relatively high accelerations and sometimes erratic motion.

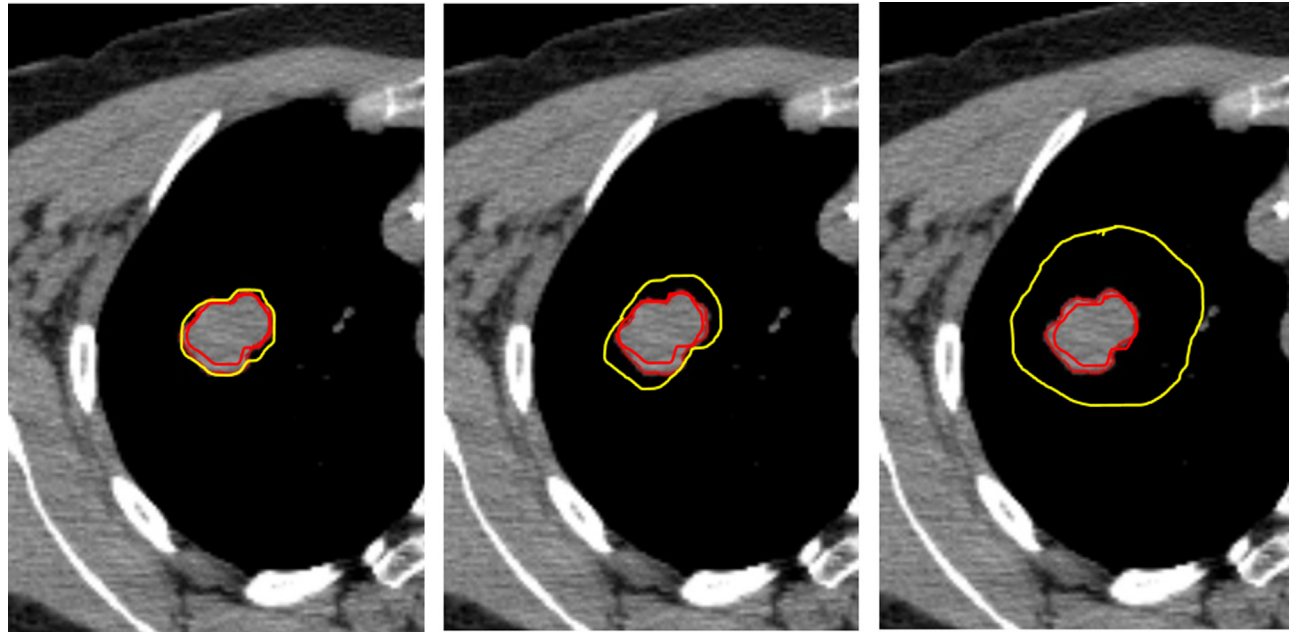


**FIGURE 2.9** An example CTV (purple contour) to PTV (yellow contour) expansion for 2-view (left), 1-view (middle), and 0-view (right) Xsight lung tracking. In the 2-view case the positional uncertainty, and therefore the CTV–PTV margin is minimized. In the 1-view case shown in this example, the tumor can be localized using the X-ray source located at the top-right of the image but not the one at the top-left. Therefore a larger margin is needed normal to the projection of the top-right X-ray source image to account for the positional uncertainty in this direction. Note that this margin does not represent the entire range of motion in this direction, since the uncertainty is constrained by tracking the motion in the other projection. In the 0-view case the margin accounts for the full range of respiratory motion and intrafraction uncertainty in the position of the tumor relative to the spine, since only the spine is aligned during treatment. CTV, Clinical target volume; PTV, planning target volume.

Of the image registration methods in [Section 2.3.4.1](#), fiducial marker tracking, Xsight lung, and Xsight spine (the latter for spinal targets treated in the prone position) can be combined with Synchrony. Immediately prior to treatment X-ray images are acquired at multiple phases of the breathing cycle and the external marker (scalar) positions are captured at the same instants. For each optical marker, a correlation model is fitted to these external marker positions versus tumor position data, with a separate model generated for superior–inferior, anterior–posterior, and left–right tumor motion components. During treatment delivery, the markers are monitored continuously, and tumor position is estimated in real time using the average of the correlation model outputs associated with each visible marker. The 3D offset of this position from the static tumor position in the treatment plan is applied by the robotic treatment manipulator in real time.

The main complications of tracking respiratory motion using an internal–external correlation model are (1) the correlation between internal and external motion may be nonlinear due to hysteresis in lung inflation/deflation and nonzero phase difference between external and internal chest motion [35,36], (2) the correlation may not be stable between, or during, treatment sessions [35–37], and (3) the treatment manipulator cannot respond instantaneously to a requested change in position. The first of these problems is addressed by fitting multiple correlation models, including linear and nonlinear functions to the internal–external position data, and automatically selecting between them using a measure of the fit quality. The second problem is greatly reduced because the correlation model is built immediately prior to each treatment session using data acquired at that time, so there is no assumption that any prior motion data (say from a planning 4D-CT or from previous treatment sessions) is representative of the motion pattern today. The problem of intra-treatment model stability is mitigated by acquiring new images throughout treatment, and using these new internal–external position data to continually adapt the correlation model. Fifteen model points are used in a first-in first-out method to construct each model. When a new model point is acquired the external marker signal is used to synchronize the X-ray acquisition such that the new point corresponds to the same phase of the breathing cycle as the data point about to be ejected. Finally, the third complication is minimized by reducing the latency period as much as possible, to 115 ms in the current system. The tumor may still move as much as 2 mm during this period, and so a prediction algorithm is required to convert the output of the correlation model to an instant 115 ms in the future. This algorithm uses a combination of pattern matching (searching the history of correlation model outputs for the pattern



found just before each instant, and using this to predict the output 115 ms later) and a least mean square prediction, with preference usually given to the former. A more detailed description is given by Sayeh et al. [38].

### 2.3.5 Image registration and segmentation algorithms for treatment planning

During treatment planning, a 3D CT image of the patient must be imported to the TPS. This CT, referred to as the primary image, is mandatory because it allows construction of the DRRs required for tracking during treatment delivery (see [Section 2.3.4.1](#)) and calculation of tissue properties needed for radiation dose calculation (see [Section 2.3.6.1](#)). An important additional role of this CT image is to enable segmentation of the target volume(s) and relevant organs at risk (OARs), which are needed to construct and evaluate the treatment plan (see [Section 2.3.6.2](#)). CT is not the optimal imaging modality for segmenting all structures, and the amount of manual work in image segmentation can form a large part of the treatment planning process. Therefore the TPS enables the user to import multiple secondary images and coregister them to the primary CT image to assist with segmentation, and provides tools for automated segmentation of some anatomies.

#### 2.3.5.1 Multimodality image import and registration

Up to five secondary 3D image sets (or 15 if multiple phases of 4D-CT are used) can be imported into any treatment plan. The most common secondary images include MRI, CT with contrast enhancement, and multiple phases from a 4D-CT series. Tools are provided to rigidly or deformably register these secondary images to the primary CT image. The simplest option is to indicate that the images are already coregistered, which may, for example, be the case if the primary CT is acquired using a PET–CT scanner and the secondary image is a PET scan acquired at the same time. This option might also be used if third-party software has already been used to register the two images. Rigid registration is performed using an intensity-based (normalized mutual information) similarity measure. The user has the option of guiding the registration result by manually defining seed points in the two images, or of omitting the intensity-based registration entirely and registering only on the seed points. For intensity-based registration the user may limit the calculation to a subvolume of the images (e.g., to a region around the tumor if the secondary image will only be used to guide the tumor segmentation).

Deformable image registration uses a proprietary nonrigid algorithm. The algorithm assumes no specific parameterization of the deformation field but instead estimates it independently at discrete points, subject to smoothness regularization. The algorithm uses an intensity-based similarity measure (normalized cross-correlation) calculated over small patches, and the deformation field is optimized iteratively in a coarse to fine resolution sequence with smoothness regularization applied during each iteration (typically three or four resolution levels and up to 500 iterations per level). The algorithm is implemented on graphics processing unit (GPU) and typically takes 20–30 seconds to register two  $512 \times 512 \times 300$  images. The algorithm and its validation are described elsewhere [39,40]. The registration result from any secondary image can be copied to any other. For example, the same registration can be applied to all phases of a 4D-CT, or if the CT component of a PET–CT study is registered to the primary image, then the same registration can be applied to the PET component.

#### 2.3.5.2 Automated image segmentation

The deformable image registration method is also used to perform autosegmentation of healthy anatomy within the primary image by registering it to multiple presegmented atlases. Specifically, autosegmentation tools are provided for brain (which requires a T1w patient MR registered to the primary CT image) and head and neck anatomies [39]. Brain autosegmentation uses a library of 50 segmented MR scans, each containing 157 structures manually defined by a neuroanatomist (including cortical parcellations). The 20 most similar atlases to any patient image are automatically selected and deformably registered to the patient image, the process typically taking about 3 minutes ([Fig. 2.10](#)). Majority voting is used to allocate each voxel in the patient image to one of the atlas structures. The head and neck autosegmentation tool uses a similar approach to segment 15 structures. A different autosegmentation approach is provided for the male pelvic anatomy, which combines aspects of model-based and atlas-based methods to segment seven structures, including prostate, seminal vesicles, urethra, bladder, and rectum, using the primary CT image. All automatically segmented VOIs can be reviewed and manually edited.

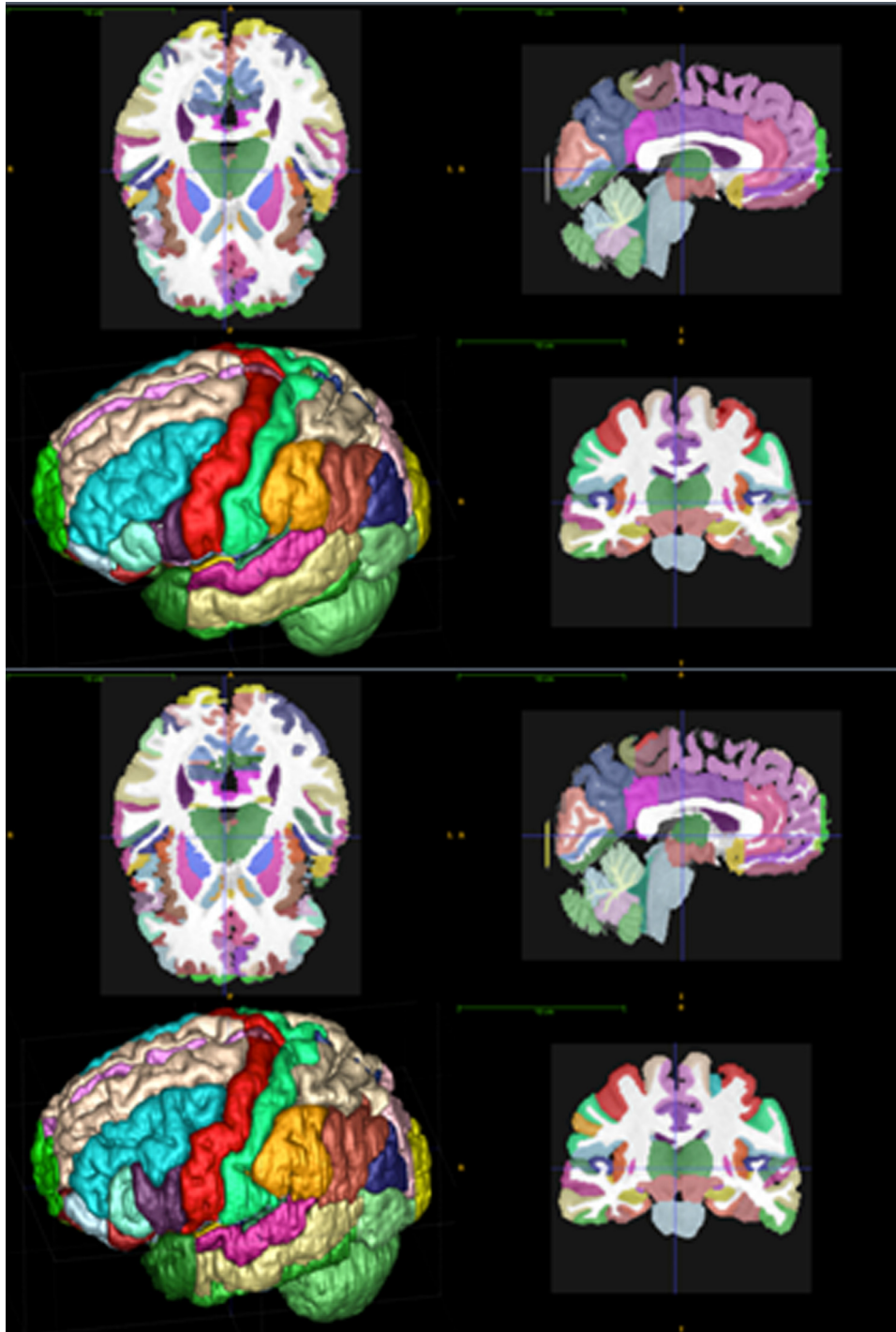


**FIGURE 2.10** Autosegmented brain structures (top) versus manually segmented structures (bottom). This leave-one-out comparison was performed by taking one of 20 expert atlases as an estimate of the ground truth, and comparing against autosegmentation of this image using the deformable registration method applied to the other 19 atlases. Auto- and manually segmented structures were compared using mean surface distance, with results varying from 0.3 mm (Brainstem, Optic Chiasm, Putamen, Pallidum, Ventral Diencephalon) to 1.1 mm (Postcentral Gyrus).

### 2.3.5.3 Retreatment

Another use of deformable registration is for situations where a patient requires treatment using CyberKnife having already received radiation therapy (delivered using CyberKnife or some other treatment delivery system) to the same, or an adjacent, anatomical region. In these cases, it can be important to visualize the dose distribution of the new treatment in combination with that delivered previously in order to properly assess the complication risks and optimize the new treatment plan. The retreatment functionality provided by the TPS allows the new primary CT to be deformably registered to the planning CT image from the previous treatment. This registration is then used to overlay the isodose

line representations of the previous treatment onto the new primary image and convert these into VOIs that can be used to guide the dose optimization in the new plan. For example, it is possible to identify the volume of an OAR in the new plan which received more than a certain dose previously (this volume is the intersection of the OAR in the new CT, with the corresponding isodose deformably registered from the prior treatment CT), and ensure that the dose in this region is constrained to a safe level in the new plan.

### 2.3.6 Radiation dose calculation and optimization algorithms for treatment planning

#### 2.3.6.1 Dose calculation algorithms

The dose calculation problem involves modeling the interaction of primary X-ray photons within the patient, and the energy deposition of secondary electrons generated by these interactions. Dose calculation algorithms are often differentiated by whether the secondary electron transport is considered explicitly (type B algorithm) or energy deposition is considered to be a constant proportion of photon energy lost in each voxel (type A). For many clinical applications, these two methods have equivalent accuracy. The major exception is for small beams inside low-density organs (such as lung) or at the interfaces between soft tissues and low-density materials (such as tumor–lung or tumor–air interfaces). In these cases, type A algorithms can result in dose calculation errors of 10% or more (Fig. 2.11).

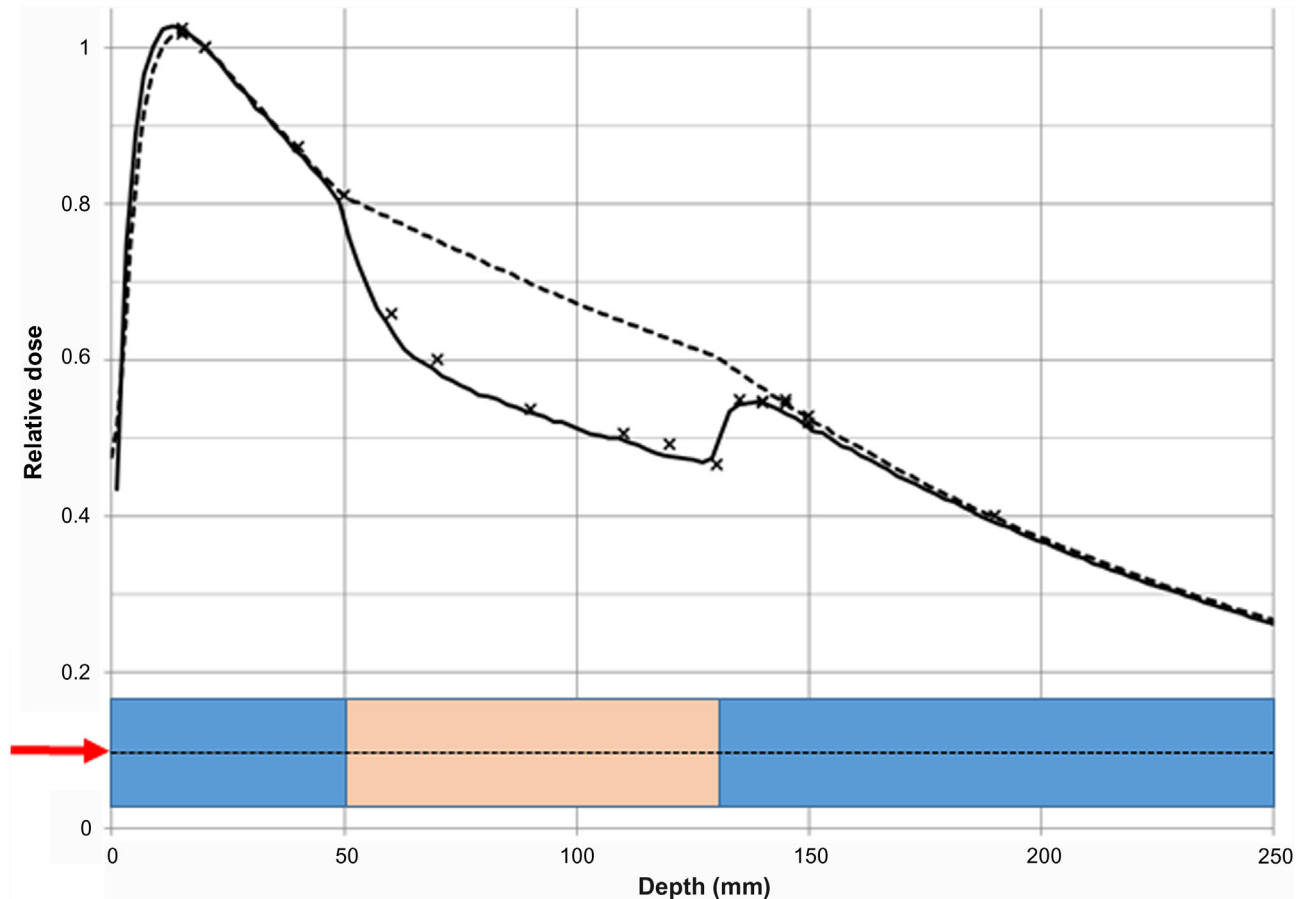


**FIGURE 2.11** A comparison of dose measurements (×) and calculations using the type A FSPB algorithm without lateral kernel scaling (dotted line) and the type B Monte Carlo algorithm (solid line) along the beam central axis of a 15.4 mm × 15.4 mm MLC beam. Relative dose (normalized at 20 mm depth) is plotted as a function of depth along the central axis. As shown in the figure, the beam (indicated by the red arrow) is normally incident onto a phantom containing 5 cm of water-equivalent plastic, followed by 8 cm of lung-equivalent plastic, and then another 15 cm of water-equivalent plastic. Within the water-equivalent material, which has similar radiation absorption and scattering properties to most soft tissues, both calculations agree well with measurement. However, within the lung material, and just downstream of the lung–water interface, the type A algorithm overestimates the dose while the type B algorithm maintains a good agreement with the measurement. FSPB, Finite-size pencil beam.

**TABLE 2.1** Type A and B dose calculation algorithms provided for CyberKnife circular (fixed and Iris collimators) and irregular (multileaf collimator) apertures.

	Type A algorithm	Type B algorithm
Fixed and Iris collimators	Ray-trace	Monte Carlo
Multileaf collimator	Finite-size pencil beam	Monte Carlo

The CyberKnife TPS includes type A and B algorithms (Table 2.1). The ray-tracing algorithm is an example of a type A tabulated beam data algorithm [41], and relies on a large set of stored data obtained from dose measurements made in a uniform water phantom to reconstruct the dose at any point within a patient. These data are measured for each of the 12 possible field sizes during system commissioning. This approach is not applicable to the MLC because of the infinite number of possible apertures that can be formed. Instead, a pencil beam algorithm (also type A) generates the dose distribution by the weighted summation of kernels distributed across an arbitrary 2D beam aperture, that each represent the dose distribution delivered by a narrow pencil beam in an infinite water phantom [41]. The specific finite-size pencil beam (FSPB) algorithm employed is described elsewhere [42]. For both algorithms, the effect of density variations (i.e., to compensate for the fact that the patient is not uniformly water equivalent) on photon energy loss is modeled using *equivalent path length*, where the effective depth along a ray-line linking the X-ray source to the dose calculation point is calculated as the integral of relative electron density along the ray (electron density at each voxel/electron density of water). The FSPB algorithm accuracy can be further improved in low-density materials by scaling the kernels laterally based on local density to simulate the extended electron range [43], which is implemented as an option.

The type B algorithm provided is Monte Carlo dose calculation [44–48]. In this approach the interactions of individual primary photons, and of secondary electrons and photons generated in these initial interactions, are explicitly simulated. This is a stochastic process since only the probabilities of individual interactions can be known, and therefore the dose calculation involves simulating many thousands of incident photons to achieve a result with acceptable random uncertainty at each voxel.

Ray-trace and FSPB dose calculations are faster (requiring just a few seconds) in comparison to Monte Carlo (which calculates a typical MLC lung treatment plan with 2% uncertainty in 1–2 minutes [48]). Most commonly, type A algorithms are used for clinical applications other than lung cancer and some head and neck cancers, where type B algorithms are preferred. The type B algorithms can be used for final dose calculation to minimize the dose prescription error, and for preoptimization dose calculation to minimize the optimization convergence error [49]. The most appropriate use of type B algorithms in this context is somewhat contentious [50,51], and so it is important that the user retains control over the algorithm selection at each stage of treatment planning.

### 2.3.6.2 Dose optimization algorithms

During radiation treatment plan optimization, the planner determines how to apply the delivery system to treat a specific patient. The inputs are the segmented patient anatomy, possible beam orientations, dose calculations for those beams, and the objectives for the patient treatment. The output is the geometry and fluence distribution of radiation beams that most closely achieve those objectives.

The CyberKnife TPS includes two optimization methods, sequential optimization (SO) and VOLO. For both methods, the user can set objectives on the dose to segmented anatomical regions, such as tumors and OARs, the dose delivered to artificial structures such as rings around the tumor or other target volumes used to control dose conformality, and the number of monitor units (MU) delivered by individual beams, summed over beams delivered from the same node, or total MU (summed over all beams).

For SO [52], the planner defines objectives which can be either constraints or goals. A constraint cannot be violated during optimization. Constraints can only be set on maximum values, which guarantee that all constraints can be achieved. The maximum MU per beam and per node, if specified, are always constraints. Maximum point dose within any segmented VOI, maximum dose volume within any VOI (e.g., no more than  $X\%$  of the VOI may receive more than  $Y$  dose), and maximum total MU objectives can be treated as constraints and/or goals. Goals are objectives that can be violated. Goals may also include minimum point dose or minimum dose volume for any tumor or other VOI. In SO, the



user defines the goals in a prioritized sequence and each goal is optimized individually. The first goal to be optimized must be a minimum dose goal to a target VOI. This can be either the minimum dose to the whole volume or the minimum volume of the tumor that receives the specified dose. Once the goal, or the closest to it that is possible without violating the existing constraints, is achieved this result is converted into an additional constraint to be applied for all subsequent steps during the optimization. A small user-defined relaxation of the constraint may be defined during this conversion. The following steps in the optimization are usually ordered based on the priority of the clinical objective, with the higher priority objectives optimized before the lower priority objectives. Like the first goal, each other goal is optimized individually within the existing constraints, and its result is relaxed and the relaxed result is set as a constraint for subsequent steps.

For fixed and Iris collimators, the user selects the volumes to be targeted and the collimator diameters to use. Before optimization begins a solution space of beams is randomly generated. For the MLC, the planner selects the number of nodes to include in the optimization, the volumes to be targeted, and parameters for shape heuristics used to create individual beams. Before optimization begins, the first node is randomly selected and each additional node is chosen to maximize the spatial diversity of the current set of nodes. Shape heuristics are applied at each node to create the beams that comprise the solution space. This predetermined solution space permits formulation of the optimization as a linear programming problem, because the solution vector is the weight or MU of each beam, and MU is linearly proportional to the dose deposited in the patient, which are the values constrained or optimized. The simplex algorithm is used to solve for the optimum at each step [53].

VOLO only allows the planner to specify objectives as goals. For all collimators, the planner selects the number of nodes. As with SO, the first node is randomly determined, and subsequent nodes are calculated to maximize the spatial diversity of the current set of nodes. Also, as with SO, circular beams are randomly chosen to target the volume. For the MLC, however, the projection of the MLC is divided into rectangular pixels, called beamlets, that create a fluence map projecting from each node to each target volume. The planner manually applies a weighting factor to each clinical goal and these weighted goals are summed into a single cost function and are simultaneously optimized. The cost is formulated as a quadratic function and a quasi-Newton gradient search algorithm finds the optimal beam weights [54–60]. For circular collimators, the weights of the beams are optimized directly. For the MLC, the fluence map is initially optimized (i.e., individual beamlet weights are optimized independently). This optimization is generally performed in seconds, which allows the planner to quickly explore the solution space by varying goals and weights. Each optimal fluence map is then sequenced into deliverable apertures and the dose is recalculated using these apertures [61]. To increase the similarity between the fluence map and aperture dose distributions, the fluence optimization includes a regularization component [62] that smooths the intensities of the fluence map. After sequencing, the weight of the apertures is optimized using the same goals, weights, and search algorithm as used during fluence optimization.

Both optimizers provide dose evaluation tools such as dose volume histograms, 2D isodose lines, 3D isodose surfaces, and calculated dose statistics that allow the planner and other clinicians to determine whether the result can be approved for treatment or requires further modification.

### 2.3.7 Data management and connectivity systems

The CyberKnife treatment delivery system consists of multiple computers connected via a dedicated local area network (LAN). The system requires connection to at least one CT scanner but more typically to multiple imaging systems, information systems, and other systems distributed within the hospital and beyond. Interconnectivity is achieved using an integrated data management system (iDMS) located on the LAN. As illustrated in Fig. 2.12, iDMS acts as a central patient database capable of supporting multiple Accuray-supplied treatment delivery systems (CyberKnife, TomoTherapy, and Radixact), and the Accuray-supplied Precision TPS. In addition, it allows connection via a firewall across the hospital network to imaging systems (e.g., CT and MR scanners), hospital information systems, and picture archive and communication systems. Connectivity with third-party radiation therapy systems is enabled by interfacing with oncology information systems provided by other vendors. Connection to the hospital network also allows for additional Accuray TPS and treatment review software to be installed across the hospital. Connection of iDMS to systems beyond the hospital network is also supported via firewall, which enables remote data backup, import of imaging data from remote centers, and remote system diagnostics and service.

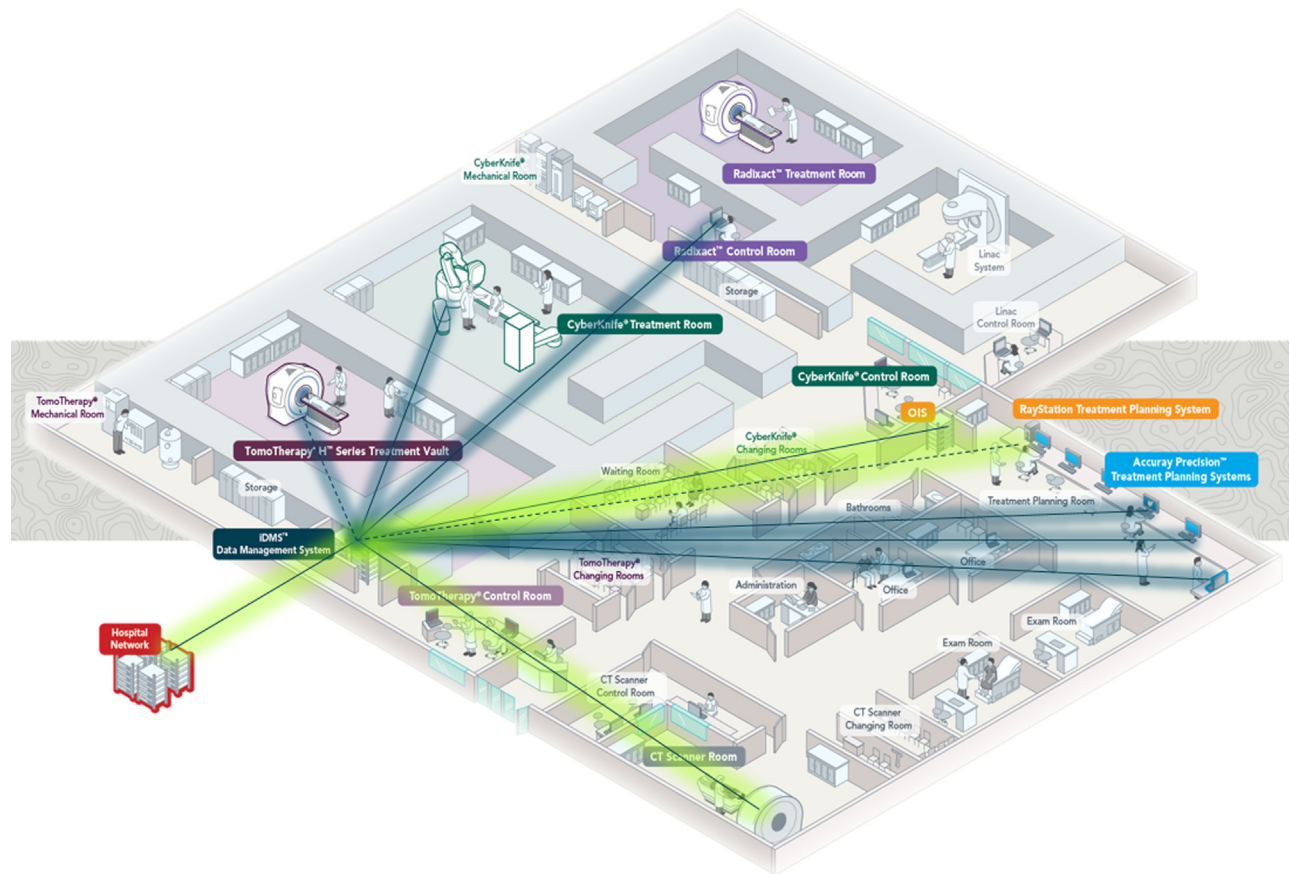


**FIGURE 2.12** The iDMS acts as a central hub for patient and treatment data used across multiple Accuray-supplied treatment systems and treatment planning systems (dark blue shaded lines) and third-party systems (light green shaded lines), including those connected to the main hospital network or external to it. iDMS, Integrated data management system.

## 2.4 Summary

The CyberKnife System is a radiation treatment system optimized for frameless radiosurgery anywhere in the body that it is clinically indicated. It provides a unique combination of robotic and image-guided technologies, and is to date the only commercial system that is custom designed for this application rather than representing a modification of an older existing treatment platform. In our previous technical review of the system in 2010 [13] we noted that while the CyberKnife System had undergone significant technical development since its initial design in the late 1990s, the basic principles of that design remained sound and were not changed. This comment can be reasserted today. As described in this chapter, since 2010 significant technical developments have been made. These include integration of a new robotic treatment manipulator and room layout to improve the available treatment workspace, development of more time-efficient methods for treatment path traversal, introduction of an MLC and associated dose calculation and optimization algorithms which improve treatment delivery and planning speed and dosimetric quality in many cases, improved methods for fiducial-less lung tumor tracking which significantly increase the proportion of patients who can benefit from this tracking method, new deformable image registration and autosegmentation methods which enable more consistent image segmentation and decreased manual workload, and improved network integration. Nevertheless, these developments have been achieved without modifying the core technical principles of the system which remain (1) minimize the CTV to PTV margin, achieved by continual image guidance, robotic treatment beam manipulation, and motion tracking (including real-time tracking of respiratory motion), and (2) minimize the treated and irradiated volumes, achieved by the large noncoplanar workspace and nonisocentric beam-targeting capabilities that are enabled by the robotic treatment manipulator, together with variable beam collimation and automated beam position/weight/shape optimization algorithms.

## Acknowledgments

The authors would like to thank their colleagues Russ Farnell, Ravi Pendse, Beth Kaplan, and Ying Xiong for their assistance with the figures.

## References

- [1] Leksell L. The stereotactic method and radiosurgery of the brain. *Acta Chir Scand* 1951;102:316–19.
- [2] Benedict SH, Yenice KM, Followill D, Galvin JM, Hinson W, Kavanagh B, et al. Stereotactic body radiation therapy: the report of AAPM Task Group 101. *Med Phys* 2010;37(8):4078–101.
- [3] Loo BW, Chang JY, Dawson LA, Kavanagh BD, Koong AC, Senan S, et al. Stereotactic ablative radiotherapy: what's in a name? *Pract Radiat Oncol* 2011;1(1):38–9.
- [4] Timmerman RD, Herman J, Cho LC. Emergence of stereotactic body radiation therapy and its impact on current and future clinical practice. *J Clin Oncol* 2014;32(26):2847.
- [5] Chin LS, Hahn SS, Patel S, Mattingly T, Kwok Y. Trigeminal neuralgia. Principles and practice of stereotactic radiosurgery. New York: Springer; 2015. p. 649–57.
- [6] Jones D. ICRU report 50—prescribing, recording and reporting photon beam therapy. *Med Phys* 1994;21(6):833–4.
- [7] Landberg T, Chavaudra J, Dobbs J, Gerard JP, Hanks G, Horiot JC, et al. Report 62. *J Int Comm Radiat Units Meas* 1999;32(1):1–52.
- [8] Kupelian P, Willoughby T, Mahadevan A, Djemil T, Weinstein G, Jani S, et al. Multi-institutional clinical experience with the Calypso System in localization and continuous, real-time monitoring of the prostate gland during external radiotherapy. *Int J Radiat Oncol Biol Phys* 2007;67(4):1088–98.
- [9] Xie Y, Djajaputra D, King CR, Hossain S, Ma L, Xing L. Intrafractional motion of the prostate during hypofractionated radiotherapy. *Int J Radiat Oncol Biol Phys* 2008;72(1):236–46.
- [10] Hoogeman MS, Nuytens JJ, Levendag PC, Heijmen BJ. Time dependence of intrafraction patient motion assessed by repeat stereoscopic imaging. *Int J Radiat Oncol Biol Phys* 2008;70(2):609–18.
- [11] Guthrie BL, Adler JJ. Computer-assisted preoperative planning, interactive surgery, and frameless stereotaxy. *Clin Neurosurg* 1992;38:112–31.
- [12] Adler Jr JR, Chang SD, Murphy MJ, Doty J, Geis P, Hancock SL. The Cyberknife: a frameless robotic system for radiosurgery. *Stereotact Funct Neurosurg* 1997;69(1–4):124–8.
- [13] Kilby W, Dooley JR, Kuduvali G, Sayeh S, Maurer Jr CR. The CyberKnife® robotic radiosurgery system in 2010. *Technol Cancer Res Treat* 2010;5:433–52.
- [14] Maciunas RJ, Galloway Jr RL, Latimer JW. The application accuracy of stereotactic frames. *Neurosurgery* 1994;35(4):682–95.
- [15] Lin S, Kernighan BW. An effective heuristic algorithm for the traveling-salesman problem. *Oper Res* 1973;21(2):498–516.
- [16] Echner GG, Kilby W, Lee M, Earnst E, Sayeh S, Schlaefer A, et al. The design, physical properties and clinical utility of an Iris collimator for robotic radiosurgery. *Phys Med Biol* 2009;54(18):5359.
- [17] Asmerom G, Bourne D, Chappelow J, Goggin LM, Heitz R, Jordan P, et al. The design and physical characterization of a multileaf collimator for robotic radiosurgery. *Biomed Phys Eng Express* 2016;2(1):017003.
- [18] Murphy MJ, Balter J, Balter S, BenComo Jr JA, Das IJ, Jiang SB, et al. The management of imaging dose during image-guided radiotherapy: report of the AAPM Task Group 75. *Med Phys* 2007;34(10):4041–63.
- [19] Galanski M, Nagel HD, Stamm G. Expositions-dosis bei CT-Untersuchungen: Ergebnisse einer bundesweiten Umfrage. *RöFo* 2000;172:M164–8.
- [20] Fiberg EG. Norwegian radiation protection authority. Østerås, Norway: Department of Radiation Protection and Nuclear Safety; 2000. p. 193–6.
- [21] Smith-Bindman R, Lipson J, Marcus R, Kim KP, Mahesh M, Gould R, et al. Radiation dose associated with common computed tomography examinations and the associated lifetime attributable risk of cancer. *Arch Intern Med* 2009;169(22):2078–86.
- [22] de González AB, Mahesh M, Kim KP, Bhargavan M, Lewis R, Mettler F, et al. Projected cancer risks from computed tomographic scans performed in the United States in 2007. *Arch Intern Med* 2009;169(22):2071–7.
- [23] Fu D, Kuduvali G. A fast, accurate, and automatic 2D–3D image registration for image-guided cranial radiosurgery. *Med Phys* 2008;35(5):2180–94.
- [24] Fu D, Kuduvali G. Enhancing skeletal features in digitally reconstructed radiographs. *Medical imaging 2006: image processing*, vol. 6144. International Society for Optics and Photonics; 2006. p. 61442M.
- [25] Fu D, Kuduvali G, Maurer CR, Allison JW, Adler JR. 3D target localization using 2D local displacements of skeletal structures in orthogonal X-ray images for image-guided spinal radiosurgery. *Int J Comput Assist Radiol Surg* 2006;1:198–200.
- [26] Ho AK, Fu D, Cotrutz C, Hancock SL, Chang SD, Gibbs IC, et al. A study of the accuracy of Cyberknife spinal radiosurgery using skeletal structure tracking. *Oper Neurosurg* 2007;60(Suppl. 2):ONS-147.
- [27] Anantham D, Feller-Kopman D, Shanmugham LN, Berman SM, DeCamp MM, Gangadharan SP, et al. Electromagnetic navigation bronchoscopy-guided fiducial placement for robotic stereotactic radiosurgery of lung tumors: a feasibility study. *Chest* 2007;132(3):930–5.
- [28] Reichner CA, Collins BT, Gagnon GJ, Malik S, Jamis-Dow C, Anderson ED. The placement of gold fiducials for CyberKnife stereotactic radiosurgery using a modified transbronchial needle aspiration technique. *J Bronchol Interv Pulmonol* 2005;12(4):193–5.

- [29] Murphy MJ. Fiducial-based targeting accuracy for external-beam radiotherapy. *Med Phys* 2002;29(3):334–44.
- [30] Mu Z, Fu D, Kuduvali G. Multiple fiducial identification using the hidden Markov model in image guided radiosurgery. In: *Computer vision and pattern recognition workshop*, 2006. CVPRW'06. IEEE; Conference on June 17; 2006. pp. 92–92.
- [31] Hatipoglu S, Mu Z, Fu D, Kuduvali G. Evaluation of a robust fiducial tracking algorithm for image-guided radiosurgery. *Medical imaging 2007: visualization and image-guided procedures*, vol. 6509. International Society for Optics and Photonics; 2007. p. 65090A.
- [32] Mu Z, Fu D, Kuduvali G. A probabilistic framework based on hidden Markov model for fiducial identification in image-guided radiation treatments. *IEEE Trans Med Imaging* 2008;27(9):1288–300.
- [33] Fu D, Kahn R, Wang B, Wang H, Mu Z, Park J, et al. Xsight lung tracking system: a fiducial-less method for respiratory motion tracking. Treating tumors that move with respiration. Berlin, Heidelberg: Springer; 2007. p. 265–82.
- [34] Jordan P, West J, Sharda A, Maurer C. SU-GG-J-24: retrospective clinical data analysis of fiducial-free lung tracking. *Med Phys* 2010;37(6 Part 9):3150.
- [35] Seppenwoolde Y, Shirato H, Kitamura K, Shimizu S, Van Herk M, Lebesque JV, et al. Precise and real-time measurement of 3D tumor motion in lung due to breathing and heartbeat, measured during radiotherapy. *Int J Radiat Oncol Biol Phys* 2002;53(4):822–34.
- [36] Shirato H, Seppenwoolde Y, Kitamura K, Onimura R, Shimizu S. Intrafractional tumor motion: lung and liver. In: *Seminars in radiation oncology* (vol. 14, no. 1, pp. 10–18). WB Saunders; 2004.
- [37] Keall PJ, Mageras GS, Balter JM, Emery RS, Forster KM, Jiang SB, et al. The management of respiratory motion in radiation oncology report of AAPM Task Group 76 a. *Med Phys* 2006;33(10):3874–900.
- [38] Sayeh S, Wang J, Main WT, Kilby W, Maurer CR. Respiratory motion tracking for robotic radiosurgery. Treating tumors that move with respiration. Berlin, Heidelberg: Springer; 2007. p. 15–29.
- [39] Jordan P, Myronenko A, Gorczowski K, Foskey M, Holloway R, Maurer Jr. CR. Accuray® deformable image registration: evaluation and description (white paper). Sunnyvale, CA: Accuray Inc.; 2017.
- [40] Gupta V, Wang Y, Romero AM, Myronenko A, Jordan P, Maurer C, et al. Fast and robust adaptation of organs-at-risk delineations from planning scans to match daily anatomy in pre-treatment scans for online-adaptive radiotherapy of abdominal tumors. *Radiother Oncol* 2018;127(2):332–8.
- [41] Rosenwald JC, Rosenberg I, Shentall G. Patient dose computation for photon beams. *Handbook of radiotherapy physics—theory and practice*. Taylor & Francis; 2007. p. 559–85.
- [42] Jeleń U, Söhn M, Alber M. A finite size pencil beam for IMRT dose optimization. *Phys Med Biol* 2005;50(8):1747.
- [43] Jeleń U, Alber M. A finite size pencil beam algorithm for IMRT dose optimization: density corrections. *Phys Med Biol* 2007;52(3):617.
- [44] Ma CM, Li JS, Deng J, Fan J. Implementation of Monte Carlo dose calculation for CyberKnife treatment planning. In: *Journal of physics: conference series* (vol. 102, no. 1). IOP Publishing; 2008. p. 012016.
- [45] Wilcox EE, Daskalov GM. Accuracy of dose measurements and calculations within and beyond heterogeneous tissues for 6MV photon fields smaller than 4cm produced by Cyberknife. *Med Phys* 2008;35(6 Part 1):2259–66.
- [46] Muniruzzaman M, Dooley J, Kilby W, Lee M, Maurer C, Sims C. WE-E-AUD B-02: validation tests for CyberKnife® Monte Carlo dose calculations using heterogeneous phantoms. *Med Phys* 2008;35(6 Part 24):2953.
- [47] Marijnissen H, Hol M, van der Baan P, Heijmen B. Verification of Monte Carlo dose calculations in an anthropomorphic thorax phantom for Cyberknife treatment of small lung tumors. In: *Radiotherapy and oncology* (vol. 88); 2008. pp. S114–5.
- [48] Dooley JR, Noll JM, Kilby W, Fong W, Yeung T, Goggin LM, et al. Abstract ID: 145 Monte Carlo for CyberKnife radiosurgery with the InCise multileaf collimator. *Phys Med* 2017;42:31.
- [49] Jeraj R, Keall PJ, Siebers JV. The effect of dose calculation accuracy on inverse treatment planning. *Phys Med Biol* 2002;47(3):391.
- [50] Hoogeman MS, van de Water S, Levendag PC, van der Holt B, Heijmen BJ, Nuytens JJ. Clinical introduction of Monte Carlo treatment planning: a different prescription dose for non-small cell lung cancer according to tumor location and size. *Radiother Oncol* 2010;96(1):55–60.
- [51] Lacomberie T, Lisbona A, Mirabel X, Lartigau E, Reynaert N. GTV-based prescription in SBRT for lung lesions using advanced dose calculation algorithms. *Radiat Oncol* 2014;9(1):223.
- [52] Schlaefel A, Schweikard A. Stepwise multi-criteria optimization for robotic radiosurgery. *Med Phys* 2008;35(5):2094–103.
- [53] Dantzig GB. *Linear programming and extensions*. Princeton, NJ: Princeton University Press, 1963. ISBN-13: 978-0691059136.
- [54] Broyden CG. The convergence of a class of double-rank minimization algorithms 1. General considerations. *IMA J Appl Math* 1970;6(1):76–90.
- [55] Fletcher R. A new approach to variable metric algorithms. *Comput J* 1970;13(3):317–22.
- [56] Goldfarb D. A family of variable-metric methods derived by variational means. *Math Comput* 1970;24(109):23–6.
- [57] Shanno DF. Conditioning of quasi-Newton methods for function minimization. *Math Comput* 1970;24(111):647–56.
- [58] Byrd RH, Lu P, Nocedal J, Zhu C. A limited memory algorithm for bound constrained optimization. *SIAM J Sci Comput* 1995;16(5):1190–208.
- [59] Zhu C, Byrd RH, Lu P, Nocedal J. Algorithm 778: L-BFGS-B: Fortran subroutines for large-scale bound-constrained optimization. *ACM Trans Math Softw (TOMS)* 1997;23(4):550–60.
- [60] Morales JL, Nocedal J. Remark on “Algorithm 778: L-BFGS-B: Fortran subroutines for large-scale bound constrained optimization”. *ACM Trans Math Softw (TOMS)* 2011;38(1):7.
- [61] Xia P, Verhey LJ. Multileaf collimator leaf sequencing algorithm for intensity modulated beams with multiple static segments. *Med Phys* 1998;25(8):1424–34.
- [62] Carlsson F, Forsgren A. Iterative regularization in intensity-modulated radiation therapy optimization. *Med Phys* 2006;33(1):225–34.